



Calhoun: The NPS Institutional Archive
DSpace Repository

Theses and Dissertations

1. Thesis and Dissertation Collection, all items

2020-03

HYBRID SHIP HESS ENERGY MANAGEMENT SYSTEM DESIGN USING MPC

Tan, Wei Sheng Wilson

Monterey, CA; Naval Postgraduate School

<http://hdl.handle.net/10945/64885>

Downloaded from NPS Archive: Calhoun



Calhoun is a project of the Dudley Knox Library at NPS, furthering the precepts and goals of open government and government transparency. All information contained herein has been approved for release by the NPS Public Affairs Officer.

Dudley Knox Library / Naval Postgraduate School
411 Dyer Road / 1 University Circle
Monterey, California USA 93943

<http://www.nps.edu/library>



NAVAL POSTGRADUATE SCHOOL

MONTEREY, CALIFORNIA

THESIS

HYBRID SHIP HESS ENERGY MANAGEMENT SYSTEM DESIGN USING MPC

by

Wei Sheng Wilson Tan

March 2020

Thesis Advisor:
Co-Advisor:
Second Reader:

Roberto Cristi
Giovanna Oriti
Arthur J. Krener

Approved for public release. Distribution is unlimited.

THIS PAGE INTENTIONALLY LEFT BLANK

REPORT DOCUMENTATION PAGE			<i>Form Approved OMB No. 0704-0188</i>	
Public reporting burden for this collection of information is estimated to average 1 hour per response, including the time for reviewing instruction, searching existing data sources, gathering and maintaining the data needed, and completing and reviewing the collection of information. Send comments regarding this burden estimate or any other aspect of this collection of information, including suggestions for reducing this burden, to Washington headquarters Services, Directorate for Information Operations and Reports, 1215 Jefferson Davis Highway, Suite 1204, Arlington, VA 22202-4302, and to the Office of Management and Budget, Paperwork Reduction Project (0704-0188) Washington, DC 20503.				
1. AGENCY USE ONLY (Leave blank)		2. REPORT DATE March 2020		3. REPORT TYPE AND DATES COVERED Master's thesis
4. TITLE AND SUBTITLE HYBRID SHIP HESS ENERGY MANAGEMENT SYSTEM DESIGN USING MPC			5. FUNDING NUMBERS	
6. AUTHOR(S) Wei Sheng Wilson Tan				
7. PERFORMING ORGANIZATION NAME(S) AND ADDRESS(ES) Naval Postgraduate School Monterey, CA 93943-5000			8. PERFORMING ORGANIZATION REPORT NUMBER	
9. SPONSORING / MONITORING AGENCY NAME(S) AND ADDRESS(ES) N/A			10. SPONSORING / MONITORING AGENCY REPORT NUMBER	
11. SUPPLEMENTARY NOTES The views expressed in this thesis are those of the author and do not reflect the official policy or position of the Department of Defense or the U.S. Government.				
12a. DISTRIBUTION / AVAILABILITY STATEMENT Approved for public release. Distribution is unlimited.			12b. DISTRIBUTION CODE A	
13. ABSTRACT (maximum 200 words) A ship experiences different sea conditions during sailing. Particularly in adverse conditions, the ship generator will be put under extreme loading stress due to power fluctuations. This could potentially damage or shut down the generator. Having a Hybrid Energy Storage System (HESS) reduces the loading stress on the generator, as it can take over as an alternative power source. The goal of the thesis is to design a control strategy using Model Predictive Control (MPC) to effectively control the HESS output behaviors in order to compensate for power fluctuations due to ocean waves. For the purpose of this thesis, the HESS is composed of a combination of batteries and supercapacitors. Computer simulation using MATLAB verified that the MPC is able to effectively control the HESS in compensating for power fluctuations and at the same time, minimize generator overload. Different weightages on the battery were also tested to observe the battery and supercapacitor output behaviors. The simulation also provided insight into the impact of the weightages on the states and inputs, and it was observed that there is saturation on the battery and supercapacitor currents when their weightage difference is greater than 20. In addition, the model could also be used for preliminary study for HESS sizing based on the project power demands.				
14. SUBJECT TERMS energy management systems for hybrid ships, Hybrid Energy Storage System, HESS, generator overload			15. NUMBER OF PAGES 103	
			16. PRICE CODE	
17. SECURITY CLASSIFICATION OF REPORT Unclassified	18. SECURITY CLASSIFICATION OF THIS PAGE Unclassified	19. SECURITY CLASSIFICATION OF ABSTRACT Unclassified	20. LIMITATION OF ABSTRACT UU	

THIS PAGE INTENTIONALLY LEFT BLANK

Approved for public release. Distribution is unlimited.

**HYBRID SHIP HESS ENERGY MANAGEMENT SYSTEM DESIGN USING
MPC**

Wei Sheng Wilson Tan
Major, Republic of Singapore Navy
Bachelor in Mechatronics Engineering, University Of Glasgow, 2013

Submitted in partial fulfillment of the
requirements for the degree of

**MASTER OF SCIENCE IN ENGINEERING SCIENCE
(ELECTRICAL ENGINEERING)**

from the

**NAVAL POSTGRADUATE SCHOOL
March 2020**

Approved by: Roberto Cristi
Advisor

Giovanna Oriti
Co-Advisor

Arthur J. Krener
Second Reader

Douglas J. Fouts
Chair, Department of Electrical and Computer Engineering

THIS PAGE INTENTIONALLY LEFT BLANK

ABSTRACT

A ship experiences different sea conditions during sailing. Particularly in adverse conditions, the ship generator will be put under extreme loading stress due to power fluctuations. This could potentially damage or shut down the generator. Having a Hybrid Energy Storage System (HESS) reduces the loading stress on the generator, as it can take over as an alternative power source.

The goal of the thesis is to design a control strategy using Model Predictive Control (MPC) to effectively control the HESS output behaviors in order to compensate for power fluctuations due to ocean waves. For the purpose of this thesis, the HESS is composed of a combination of batteries and supercapacitors.

Computer simulation using MATLAB verified that the MPC is able to effectively control the HESS in compensating for power fluctuations and at the same time, minimize generator overload. Different weightages on the battery were also tested to observe the battery and supercapacitor output behaviors. The simulation also provided insight into the impact of the weightages on the states and inputs, and it was observed that there is saturation on the battery and supercapacitor currents when their weightage difference is greater than 20. In addition, the model could also be used for preliminary study for HESS sizing based on the project power demands.

THIS PAGE INTENTIONALLY LEFT BLANK

TABLE OF CONTENTS

I.	INTRODUCTION.....	1
II.	BACKGROUND	5
A.	ENERGY STORAGE DEVICES	5
1.	Batteries	6
2.	Supercapacitors.....	8
3.	Load Leveling and Peak Shaving	9
B.	MODEL PREDICTIVE CONTROL	10
1.	Rule-Based Strategy.....	11
2.	Optimization-Based Strategy	11
III.	PROPOSED ARCHITECTURE AND MATHEMATICAL MODELS.....	15
A.	SHIP MODEL AND SHIP DRAG (RESISTANCE)	15
1.	Drag (Resistance)	16
2.	Ship Generators	20
B.	LOAD MODEL.....	20
C.	HYBRID ENERGY STORAGE SYSTEM	21
D.	HYBRID POWERTRAIN ARCHITECTURE.....	22
1.	Diesel Generator Model.....	24
2.	HESS Model	24
IV.	RESULTS AND ANALYSIS	35
A.	LIGHT SEA CONDITIONS (15% WAVE PROFILE)	35
B.	MODERATE SEA CONDITIONS (25% WAVE PROFILE).....	41
C.	HEAVY SEA CONDITIONS (45% WAVE PROFILE).....	46
D.	ESD STATE OF CHARGE.....	52
V.	CONCLUSION AND RECOMMENDATIONS FOR FUTURE WORK.....	55
A.	CONCLUSION	55
B.	FUTURE WORK.....	56
	APPENDIX. MATLAB SCRIPT.....	57
A.	MAIN SCRIPT.....	57
B.	SHIPPOWER FUNCTION.....	65
C.	POWERSCRIPT FUNCTION	67
D.	MPCSETUP FUNCTION	73
E.	FRANCIS FUNCTION	76

LIST OF REFERENCES	79
INITIAL DISTRIBUTION LIST	85

LIST OF FIGURES

Figure 1.	Energy storage technologies. Source: [9].	6
Figure 2.	Ragone performance chart comparing the energy density, power density, and duration of energy exchange for different ESDs. Source: [25].	6
Figure 3.	Supercapacitor cell. Source: [9].	8
Figure 4.	Example of load leveling application. Source: [9].	9
Figure 5.	Peak shaving application in marine vessel. Source: [9].	10
Figure 6.	Classification of power management strategies. Source: [38].	11
Figure 7.	An illustration of MPC working principle. Source: [43].	12
Figure 8.	MF Oppedal. Source [45].	15
Figure 9.	Drag versus speed graph.	19
Figure 10.	Brake power versus speed graph.	19
Figure 11.	Illustration of the Francis equation.	32
Figure 12.	(a) $\tilde{I}_{residual}$ with q_{lbatt} and $q_{Isc} = 1$. (b) Enhanced view of the $\tilde{I}_{residual}$ initial transient response.	36
Figure 13.	(a) $\tilde{v}(t)$ with q_{lbatt} and $q_{Isc} = 1$. (b) Enhanced view of the initial transient response.	37
Figure 14.	(a) Enhanced view of the \tilde{I}_{gen} , \tilde{I}_{batt} , and \tilde{I}_{sc} output currents with q_{lbatt} and $q_{Isc} = 1$. (b) A dissected view of the individual current.	38
Figure 15.	(a) $\tilde{I}_{residual}$ with $q_{lbatt} = 30$ and $q_{Isc} = 1$. (b) Enhanced view $\tilde{I}_{residual}$ initial transient response	39
Figure 16.	(a) Enhanced view of the \tilde{I}_{gen} , \tilde{I}_{batt} and \tilde{I}_{sc} output currents with $q_{lbatt} = 30$ and $q_{Isc} = 1$. (b) A dissected view of the individual current	40
Figure 17.	(a) $\tilde{v}(t)$ with q_{lbatt} and $q_{Isc} = 1$. (b) Enhanced view of the initial transient response.	42

Figure 18.	(a) $\tilde{I}_{residual}$ with q_{lbatt} and $q_{Isc} = 1$. (b) Enhanced view of $\tilde{I}_{residual}$ initial transient response.....	43
Figure 19.	(a) Enhanced view of the \tilde{I}_{gen} , \tilde{I}_{batt} , and \tilde{I}_{sc} output currents with q_{lbatt} and $q_{Isc} = 1$. (b) A dissected view of the individual current.	43
Figure 20.	(a) $\tilde{I}_{residual}$ with $q_{lbatt} = 30$ and $q_{Isc} = 1$. (b) Enhanced view of the $\tilde{I}_{residual}$ initial transient response.....	44
Figure 21.	(a) Enhanced view of the \tilde{I}_{gen} , \tilde{I}_{batt} , and \tilde{I}_{sc} output currents with $q_{lbatt} = 30$ and $q_{Isc} = 1$	45
Figure 22.	(a) $\tilde{v}(t)$ with q_{lbatt} and $q_{Isc} = 1$. (b) Enhanced view of the initial transient response.....	47
Figure 23.	(a) $\tilde{I}_{residual}$ with q_{lbatt} and $q_{Isc} = 1$. (b) Enhanced view of $\tilde{I}_{residual}$ initial transient response.....	48
Figure 24.	(a) Enhanced view of the \tilde{I}_{gen} , \tilde{I}_{batt} , and \tilde{I}_{sc} output currents with q_{lbatt} and $q_{Isc} = 1$. (b) A dissected view of the individual current.	49
Figure 25.	(a) $\tilde{I}_{residual}$ with $q_{lbatt} = 30$ and $q_{Isc} = 1$. (b) Enhanced view of $\tilde{I}_{residual}$ initial transient response	50
Figure 26.	(a) \tilde{I}_{gen} , \tilde{I}_{batt} and \tilde{I}_{sc} output currents with $q_{lbatt} = 30$ and $q_{Isc} = 1$. (b) A dissected view of the individual current	51
Figure 27.	(a) Battery SoC. (b) SC's SoC when $q_{lbatt} = 1$	53
Figure 28.	Enhanced views of (a) Battery SoC (b) SC SoC when $q_{lbatt} = 1$	53
Figure 29.	(a) Battery SoC (b) SC SoC when $q_{lbatt} = 30$	54
Figure 30.	Enhanced views of (a) Battery SOC (b) SC SOC when $q_{lbatt} = 30$	54

LIST OF TABLES

Table 1.	The technical features of ESDs. Source: [3].	5
Table 2.	Comparison of energy delivery profile technologies. Source: [25].	7
Table 3.	A comparison between battery technologies. Source: [9].	7
Table 4.	Key specifications for MF Oppedal. Source: [46].	15
Table 5.	Specifications for lithium-ion battery. Source: [59].	21
Table 6.	Specifications for SC. Source: [60].	21
Table 7.	Weightage factors on the states and input.	28
Table 8.	Compilation of the peak output currents for \tilde{I}_{gen} , \tilde{I}_{batt} , and \tilde{I}_{sc} .	41
Table 9.	Compilation of the peak output current for \tilde{I}_{gen} , \tilde{I}_{batt} , and \tilde{I}_{sc} .	46
Table 10.	Compilation of the peak output current for \tilde{I}_{gen} , \tilde{I}_{batt} , and \tilde{I}_{sc} .	51

THIS PAGE INTENTIONALLY LEFT BLANK

LIST OF ACRONYMS AND ABBREVIATIONS

AES	All Electric Ship
CO ₂	Carbon Dioxide
EPS	Electric Propulsion System
ESD	Energy Storage Device
GHG	Green House Gas
HESS	Hybrid Energy Storage System
ICE	Internal Combustion Engine
IMO	International Maritime Organization
LDR	Length Displacement Ratio
MPC	Model Predictive Control
SC	Supercapacitor
SOC	State of Charge

THIS PAGE INTENTIONALLY LEFT BLANK

ACKNOWLEDGMENTS

First and foremost, I am extremely grateful to my parents for their love, prayers, caring, and sacrifices for educating and preparing me for my future. I am grateful for the love of my wife, Joey See. Without her love and sacrifice, my journey in NPS would have been tough. Thank you for your unwavering support and always taking care of the family and me. To my daughter Pebbles, thank you for supporting Daddy. To my soon-to-be-born daughter, Amber, welcome to the family.

Next, I would like to thank all of the teachers, professors, and staff who helped me through my wonderful and enriching NPS journey. Especially to my advisor, Dr. Roberto Cristi, and co-advisor, Dr. Giovanna Oriti, thank you for giving me the opportunity to do research and for providing invaluable guidance throughout this research. Dr. Cristi was very patient and meticulous throughout and would take his time to guide me particularly whenever the road got tough. His dynamism, vision, sincerity, and motivation have deeply inspired me. He has taught me the methodology to carry out the research and to present the research works as clearly as possible.

I would like to say thanks to my American friends. I am glad we are able to cross paths and am deeply appreciative of the warmth and friendship you guys have given to me. To the Singapore community, I will definitely miss the fun and gatherings we have had here. I will see you guys back in Singapore; meanwhile enjoy Monterey.

Finally, my gratitude goes to my commanders and colleagues, who have supported me in my work and made all this wonderful journey possible.

THIS PAGE INTENTIONALLY LEFT BLANK

I. INTRODUCTION

According to the United Nations Conference on Trade and Development (UNCTAD), the maritime industries account for 70% of world trade [1]-[3], and based on a 2012 study, the shipping industry produced about 796 million tons of carbon dioxide (CO₂) [4], [5]. Based on the projected economic growth and energy development of these industries, the International Maritime Organization (IMO) forecasts that CO₂ emissions could increase from 50% to 250% by 2050 [4]. The IMO states that to further reduce these industries environmental footprint, the IMO has proposed reducing their emissions from 3.5% to 0.5% by January 2020. It has also set targets for the shipping industry to cut down Green House Gas (GHG) emissions by at least 50% by 2050.

Technologies such as hybrid energy storage systems (HESS), variable frequency drives, and demand-side management, which are widely used in land-based microgrids and hybrid vehicles, are starting to emerge in the marine industries. While a high percentage of sea-going vessels are still diesel-powered, there is an increasing trend of ship owners and operators turning to greener technologies that can help them in reducing fuel bills and environmental impact. In particular, electrification in the marine industry has become an attractive technology, and the U.S Navy [5] has proposed the concept of an All Electric Ship (AES). Several military agencies have also embarked on AES research and designs [6]-[8]. Applying HESS in ships can generate potential benefits such as increasing flexibility in ship design, addressing power fluctuations, improving generator reliability, increasing fuel efficiency, and decreasing the CO₂ footprint.

A hybrid energy storage system is defined as a combination of two or more types of power sources/energy storage devices (ESD) that can provide energy [9]. Generally, they are classified into three categories:

1. Traditional internal combustion engines (ICE) such as diesel generators, gas, or steam turbines;
2. Electrochemical energy storage such as batteries and power sources such as fuel cells;

3. Other energy storage such as flywheels and supercapacitors.

ESDs can offer many benefits to the marine vessels. As compared to diesel engines, ESDs can quickly adapt to sudden changes in load, hence improving the stability of the overall powertrain system. Also, ESDs can reduce engine maintenance, optimize fuel consumption and minimize the power generation machinery footprint on the ship [10]. A previous thesis by Ralson [11], also examined the implementation of supercapacitors (SC) within the energy storage system of an electric propulsion system (EPS) on a hybrid-powered vessel.

ESDs are also effective in load peak shaving, load leveling, power smoothing, handling frequency and voltage fluctuations, and ensuring power quality. Development in ESDs also allows users to design a more energy-efficient ship as well as offer flexibility in power supply configuration. Unlike electric vehicles, ships can have several independently controlled energy-generating sources connected to a standard switchboard.

Several power management control strategies are commonly applied in the industry, including static optimization methods [12], [13], dynamic optimization methods [14]-[16], and predictive powertrain controls for minimizing fuel consumption [14]-[15]. With proper control strategies, the ESDs can complement each other and perform effectively. In [10], a detailed review of the types of smart ships is provided and a description of the key benefits and challenges of the different control strategies between the propulsion types.

In hybrid energy systems, the control strategy used is also a key component. A suitable control strategy that can forecast the energy demand and compute in real-time the optimal energy distribution among each ESD makes the microgrid more energy efficient.

In recent years, Model Predictive Control (MPC) has been gaining popularity in HESS energy management applications [17]. MPC is a model-based predictive control method that uses the first reference values and projects them over a prediction horizon while minimizing a cost function and satisfying a set of hard constraints on plant behavior. This recurring computation is performed based on defined intervals. MPC has been applied

in a broad range of applications, such as engine control, energy management, etc. [18]-[23].

This research studies an MPC method that minimizes the change in steady-state velocity when navigating through wave as well as minimizing the generator current by optimizing the HESS ESD output based on weightage and constraints. The MPC controls the optimal energy distribution between the available energy sources over the prediction horizon. The proposed algorithm has been simulated using a simplified dynamic model of the Norwegian car ferry, MF Oppedal [24]. The simulation results show the different tradeoffs between the energy storage devices.

This thesis is organized as follows: Chapter II introduces the types of ESDs and provides an overview of the types of control strategies. Chapter III presents the ship parameters calculations as well as the MPC state-space model. Chapter IV discusses the scenarios and simulation results. Lastly, Chapter V concludes the research and discusses areas for future work.

THIS PAGE INTENTIONALLY LEFT BLANK

II. BACKGROUND

A. ENERGY STORAGE DEVICES

The operating characteristics of various energy storage devices differ from one another in terms of technical features such as power and energy densities, charge and discharge time, operating temperature, lifetime, and maintenance requirements. Table 1 provides typical technical features of various kinds of ESDs [9].

Over the years, rapid developments in power electronics have also improved ESD capabilities. With the increasing demand for cleaner energy and lower emissions, many researchers and original equipment manufacturers are exploring the idea of combining traditional internal combustion generators with ESDs for improved efficiency.

ESDs can be classified into three main categories, i.e., electrical energy storage, chemical energy storage, and mechanical energy storage. Figure 1 shows an overview of the energy storage devices in these three categories, while Figure 2 depicts the comparison of energy density, power density, and energy exchange related to specific ESD types. It is observed that batteries have the lowest power density in terms of kWh/kg but the highest \$/kW. This could indicate that a battery would be an expensive option if a large amount of power is needed in a microgrid. The following sections will discuss in greater detail the battery and SCs operating characteristics and how they complement each other.

Table 1. The technical features of ESDs. Source: [3].

System	Power Density	Energy Density	\$/kW	Efficiency	Life Time	Response Time
	(kW/kg)	(kWh/kg)		(%)	(years)	
Lead Acid	75–300	30–50	300–600	65–80	3–15	ms
NiCd	150–300	50–75	500–1500	75–85	5–20	ms
NaS	150–230	150–240	1000–3000	75–90	10–15	ms
Li-ion	150–315	75–200	1200–4000	90–97	5–100	ms–s
Fuel Cells	500+	800–10,000	10,000+	20–50	10–30	ms–min
SMES	500–2000	0.5–5	200–300	90–95	20+	ms
Flywheel	400–1500	10–30	250–350	90–95	15–20	ms–s
Ultra-capacitor	100,000+	20+	100–300	85–98	4–12	ms

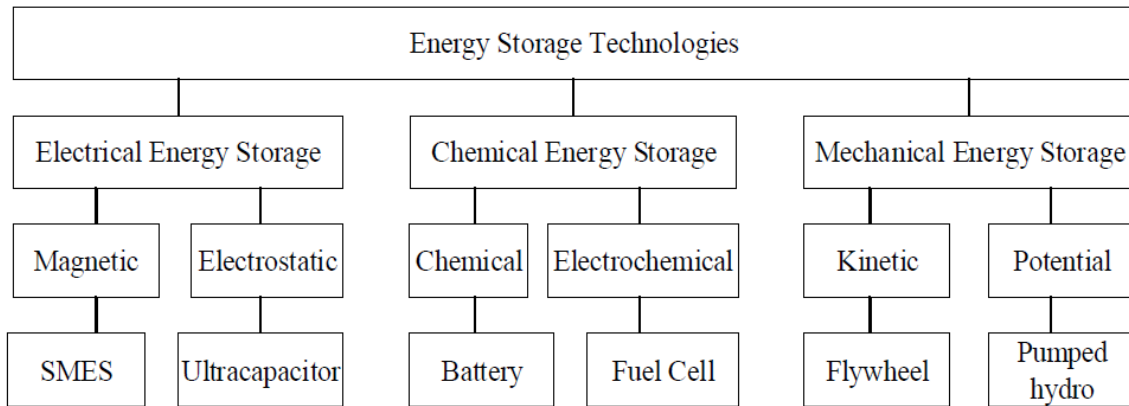


Figure 1. Energy storage technologies. Source: [9].

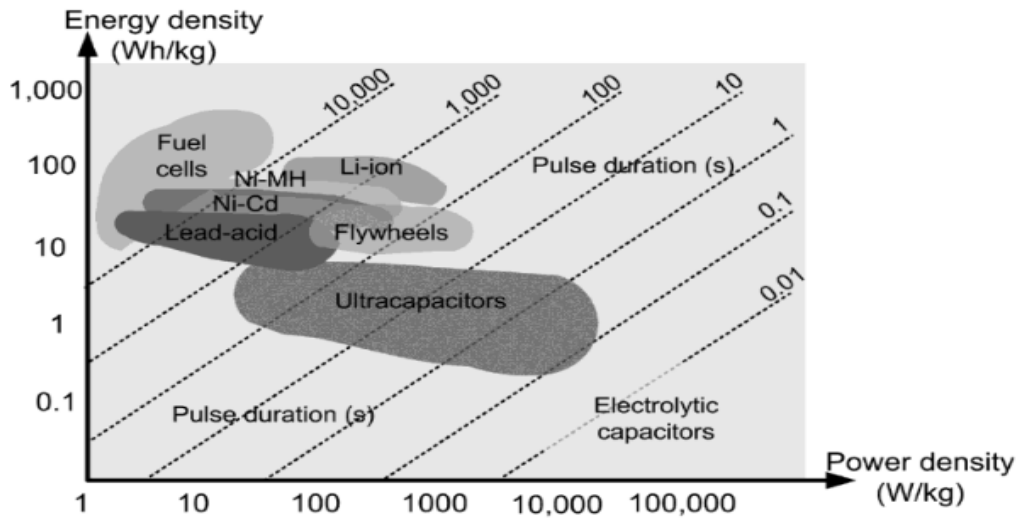


Figure 2. Ragone performance chart comparing the energy density, power density, and duration of energy exchange for different ESDs. Source: [25].

1. Batteries

Batteries transform chemical energy directly into electrical energy through an electrochemical oxidation-reduction reaction [9]. They are commonly used in Uninterruptible Power Supplies, automobiles, ships, microgrids, and other applications. In recent years, the notable increase in demand from the hybrid-electric automotive industry has led to greater demands for batteries capable of producing higher energy density. Such batteries include the lithium-ion type. Table 2 lists the technical specifications of the

lithium-ion and other types of batteries. It can be noted that a lithium-ion battery outperforms the other three batteries types, and therefore, the lithium-ion type is also the most commonly used.

Table 2. Comparison of energy delivery profile technologies. Source: [25].

	Lead-Acid	Ni-Cd	Ni-MH	Li-Ion
Cell voltage (V)	2	1.2	1.2	3.2 (LiFePO ₄)3.6 (NMC)
Specific energy (Wh/kg)	1–60	20–55	1–80	3–100
Specific power (W/kg)	<300	150–300	<200	100–1,000
Energy density (kWh/m ³)	25–60	25	70–100	80–200
Power density (MW/m ³)	<0.6	0.125	1.5–4	0.4–2
Maximum cycles	200–700	500–1,000	600–1,000	3,000
Discharge time range	>1 min	1 min–8h	>1 min	10 s–1 h
Cost (\$/kWh)	125	600	540	600
Cost (\$/kW)	200	600	1,000	1,100
Efficiency (%)	75	75	81	99

Table 3 compares the advantages and disadvantages of the different types of batteries. Although the lead-acid battery is cheaper, it has a short cycle life and very low efficiency as compared to the lithium-ion battery. In addition, the disposal of lead-acid batteries at the end of their life cycle presents challenges.

Table 3. A comparison between battery technologies. Source: [9].

Type of Battery	Advantages	Disadvantages
Lead Acid	Inexpensive Lead is easily recyclable low self-discharge (2–5% per month)	Shorty cycle-life (around 1500 cycles) Cycle life is affected by depth of charge Low energy density (about 30–50 kWh/kg)
Nickel Cadmium	High energy density (50–75 kWh/kg) High cycle count (1500–3000 cycles)	High degradation High cost Toxicity of cadmium metal
Sodium Sulphur	High energy density (150–240 kWh/kg) No self-discharge No degradation for deep charge High efficiency (75–90%)	Temperature of battery is kept between 300 °C to 350 °C
Lithium-ion	Very high efficiency (90–97%) Very low self-discharge (1–3% per month) Low maintenance	Very high cost Life cycle reduces by deep discharge Need special overcharge protection circuit

2. Supercapacitors

Supercapacitors (SC), also known as ultra-capacitors, are devices that can store large amounts of electrical charge [9]:

An SC uses two mechanisms to save electrical energy: double-layer capacitance and pseudocapacitance. Double-layer capacitance is electrostatic in origin, while pseudocapacitance is electrochemical, which means that supercapacitors combine the workings of regular capacitors with the operations of an ordinary battery. [27]

An SC also has a higher energy density than regular capacitors. Furthermore, SCs have low impedance, which enables them to supply power efficiently. They are generally applied where high energy is required for a shorter time. SCs are often paired with batteries as a complementary storage device to prolong the shelf life of the battery. Figure 3 shows the individual structure of an SC.

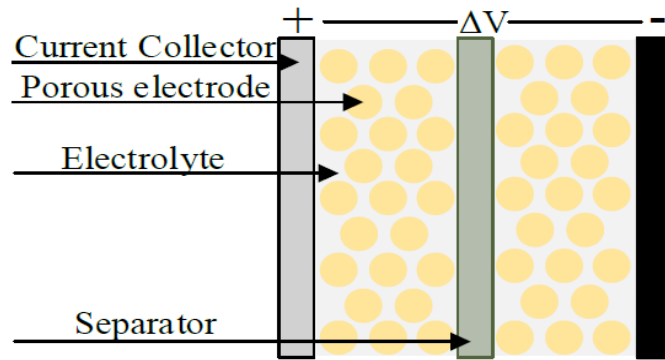


Figure 3. Supercapacitor cell. Source: [9].

Among the key features of SCs are higher power density, faster discharging and charging, and enhanced life cycle, but they often entail higher cost/Wh [9]. Other disadvantages of SCs include low energy density, high self-discharge, overcharging, and low cell voltage.

The pairing of SCs and batteries is commonly seen in hybrid vehicles [8-12] as the combination can improve the lifetime, performance, and lifecycle of the battery. This pairing has been extensively proposed in the research literature [3], [15], [16], [20],

[31]–[34]. The battery and SC complement each other well based on their contrasting energy and power densities. The SC also possesses a much longer lifecycle than the battery. This combination is usually considered for most HESS microgrids mainly due to their similarity in working principle, relatively low cost, and their complementary characteristics [9], [10]. This complementary pairing is used for matching the energy demands studied in this research project, which simulates the power demands of a ship navigating through different profiles of sea conditions.

3. Load Leveling and Peak Shaving

The creation and storage of energy during low power demand periods and the use of that energy during peak demands is defined as “load leveling” [35]. This approach is useful in reducing energy fluctuations, as shown in Figure 4. By contrast, moderating and reducing the peaks is called “peak shaving.” Figure 5 shows an illustration of peak shaving in a marine vessel. ESDs, especially batteries, have been widely adopted to cater to variable load in hybrid vehicles, and this application has been extensively researched in the literature [31], [36].

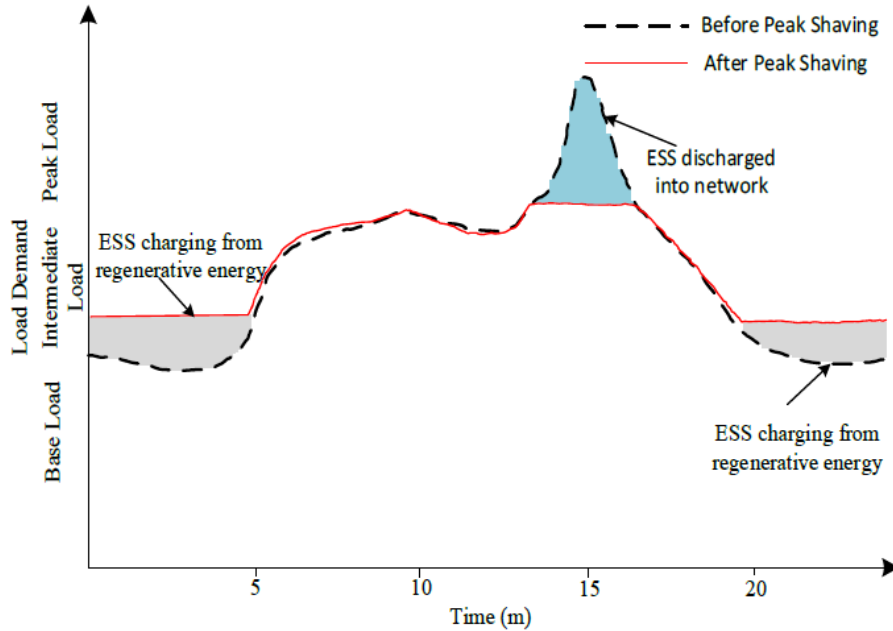


Figure 4. Example of load leveling application. Source: [9].

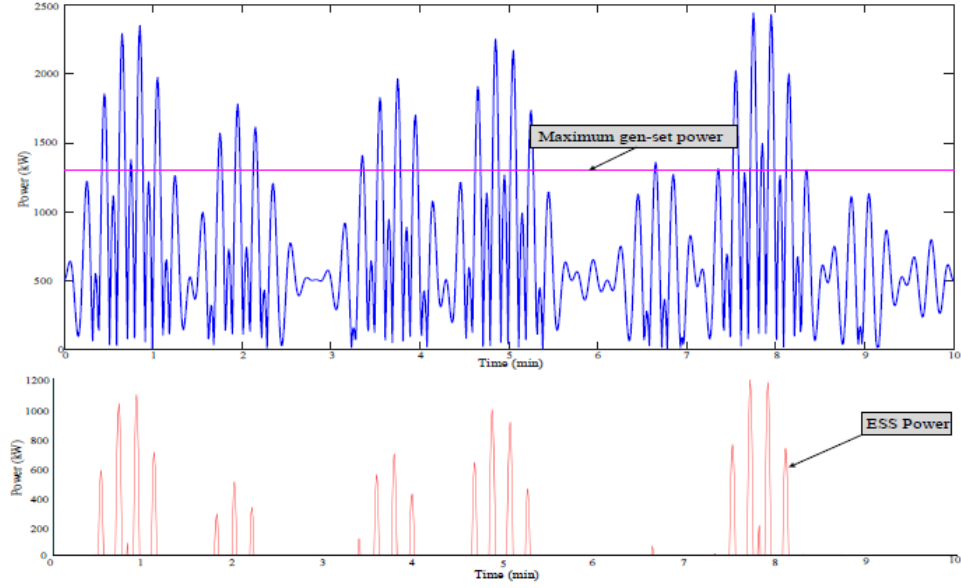


Figure 5. Peak shaving application in marine vessel. Source: [9].

B. MODEL PREDICTIVE CONTROL

The development of hybrid powertrains has been evolving rapidly in the last two decades [37]. HESS powertrains, consisting of two or more energy sources, are required to deal with different energy forms to deliver the required power demand. In this kind of system, a primary controller coordinates the energy sources so that the power demand can be satisfied efficiently and effectively. Efficient power management can lower fuel consumption and emission rates of the hybrid powertrain. In general, power management control strategies can be classified into rule-based control strategies and optimization-based control strategies [38], as illustrated in Figure 6.

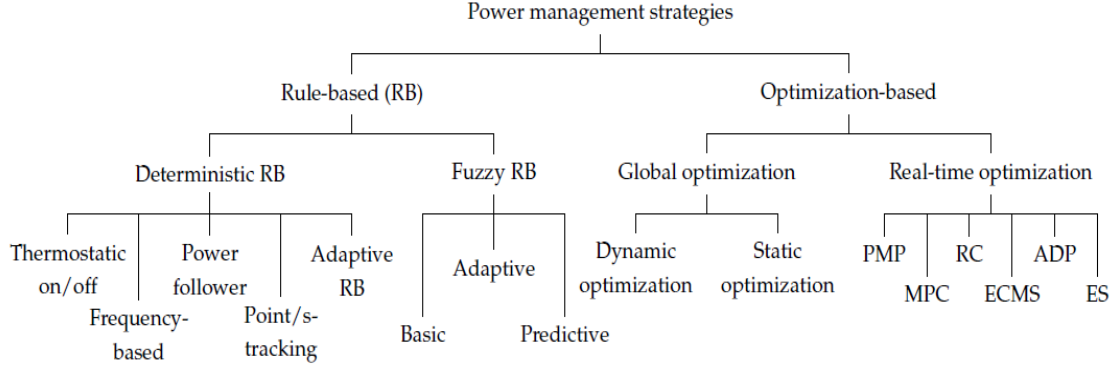


Figure 6. Classification of power management strategies. Source: [38].

1. Rule-Based Strategy

As explained in [38], rule-based techniques are ad hoc strategies in which the control law is defined by on-off or by fuzzy-logic rules [39]. Rule-based strategies are directly structured and easily implementable and are usually devised using human know-how and trial and error. Rule-based strategies are commonly used by hybrid vehicle manufacturers as this approach has low computational requirements [40]. More in-depth discussion on the different types of rule-based strategies is highlighted in [38]. It is important to note here, however, the main drawback of rule-based strategies is that they are unable to effectively react to power demands that are not defined by the rules.

2. Optimization-Based Strategy

Optimization-based strategies have been gaining more researcher attention and are also widely applied in hybrid powertrains [40]. They are based on optimal control techniques that minimize a suitable cost function, usually a quadratic function. In particular, techniques based on optimization in a finite time prediction horizon, such as the Model Predictive Control (MPC), are well known in the literature. They can be implemented in real time to provide prompt handling of power demands. For this thesis, as the load demand is dynamic and uncertain, MPC is applied as the control strategy for the hybrid powertrain.

MPC is gaining popularity and has been more widely used over the last two decades, both within the research control community and in hybrid microgrid industries

[41]. The model used for prediction is the standard discrete-time state space model of the form [42]:

$$x(t+1) = Fx(t) + Gu(t) \quad (1)$$

$$y(t) = Hx(t) + Ju(t) \quad (2)$$

Hence, at any time t and for the given state vector $x(t)$ and cost function $g(x(t), x_{t+1|t}, \dots, x_{t+N|t}, u_{t|t}, \dots, u_{t+N|t})$ associated with predicted states $x_{t+k|t} = x(t+k)$, $k=1\dots N$, and inputs $u_{t+k|t} = u(t+k)$, $k=0\dots N$, can be defined. This cost function, usually quadratic, can then be optimized with respect to the control sequence $u_{t+k|t}$, from which we determine the control $u(t) = u_{t|t}$ to be applied at the present time t .

The MPC principle is illustrated in Figure 7. As it is shown, the control input $u(t)$ at time t is based on a finite time horizon prediction based on the current state $x(t)$ and optimized with respect to future inputs $u_{t+k|t}$.

Model Predictive Control

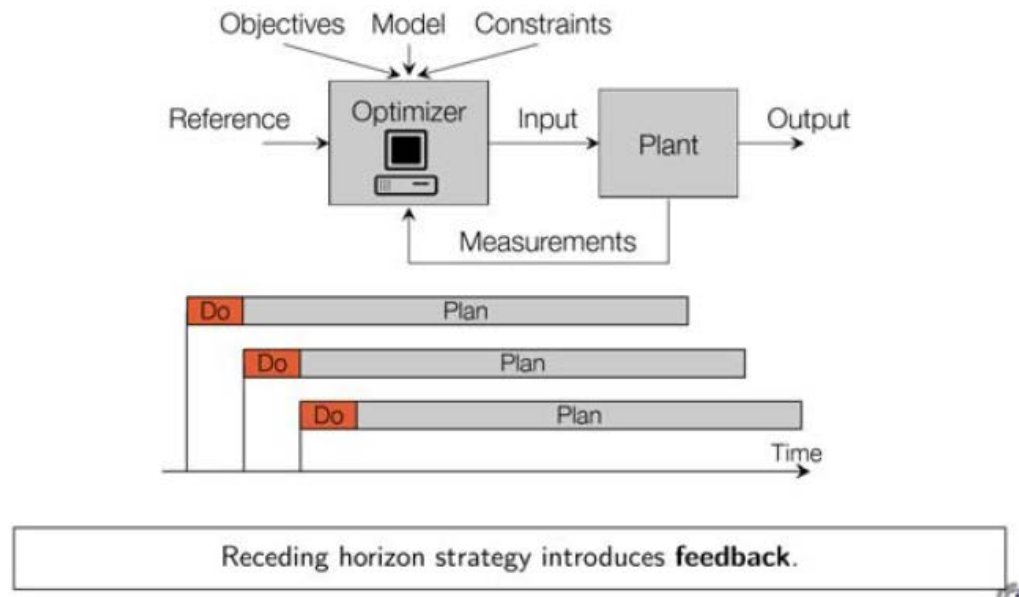


Figure 7. An illustration of MPC working principle. Source: [43].

Furthermore, MPC will also consider system limitations simply by establishing them as constraints in the optimization problem. Examples of these limitations could be the battery state of charge or the maximum charge power available in a battery [44].

For this thesis, the load model for the hybrid ship is dynamic and is supported by three energy sources. MPC enables us to determine the energy sources contribution weightage as well as to set limitations on each energy source.

THIS PAGE INTENTIONALLY LEFT BLANK

III. PROPOSED ARCHITECTURE AND MATHEMATICAL MODELS

This chapter introduces the dynamic characteristics of the various components and the proposed architecture for this research. In particular, it focuses on the dynamics of a particular ship, the MF Oppedal, which we will be using to test the effectiveness of the proposed algorithm. In addition, we will be introducing dynamic models of relevant components, such as batteries and generators, of the Hybrid Energy System. The goal is to formulate a set of state space equations and constraints, which will be used to design the optimization algorithm.

A. SHIP MODEL AND SHIP DRAG (RESISTANCE)

In this thesis, the technical specifications of the MF Oppedal are adapted to our computer simulation, along with the addition of a battery and SC as the HESS. A photograph of the MF Oppedal is shown in Figure 8 and its key specifications are listed in Table 4.



Figure 8. MF Oppedal. Source [45].

Table 4. Key specifications for MF Oppedal. Source: [46]

Ferry	Length (m)	L_{pp} (m)	Breadth (m)	Draught(m)	Velocity (Kts)
MF Oppedal	113.96	104.9	16.8	3.36	13

1. Drag (Resistance)

Any vessel underway will experience a net force opposing its forward movement due to the stress and shear forces acting on the hull surface [23]. This resistance is also known as drag. Most of the ship fuel is used to generate the required propulsive power to overcome this drag in order to propel forward. As shown in [23], Equation 4 shows the general resistance based on vessel design speed (v), wetted surface area (S), fluid density (ρ), and the resistance coefficients, (c_T).

$$R_T = \frac{1}{2} \rho_{seawater} v^2 S c_T \quad (3)$$

The total resistance coefficient c_T is given by

$$c_T = (1+k)c_F + c_R + \Delta c_F + c_{AA} \quad (4)$$

where k is the form factor, c_F is the frictional coefficient of the vessel, c_R is the residual resistance coefficient (graphical determination according to Harvald and Gulhammer [47]), Δc_F is the roughness allowance, and air resistance coefficient, c_{AA} [23].

The form factor is given by

$$k = -0.095 + 25.6(c_B / ((L_{wl} / B)^2 + (B / T)^{(1/2)})) \quad (5)$$

where L_{wl} is the length of the ship on the waterline, B is the breadth of the ship, and T is the draught of the ship. As explained in [48], the block coefficient, c_B , of the ship is given by

$$c_B = \frac{\nabla}{L_{wl} B T}, \quad (6)$$

which depicts the relationship between hull displacement ∇ and the volume in m^3 , representing the ship weight. The frictional coefficient according to the ITTC-57 model correlation line highlighted in [49] is calculated by

$$c_F = \frac{0.075}{(\log_{10} Re - 2)^2}, \quad (7)$$

where the Reynolds Number Re is calculated in relation with the viscosity η [23] as

$$Re = \frac{vL_{wl}}{\eta}. \quad (8)$$

In order to determine c_R from the Harvald and Gulhammer diagram [47], the length displacement ratio (LDR) is calculated in (9) as described in [48]:

$$LDR = \frac{L_{pp}}{\nabla^{1/3}} \quad (9)$$

As explained in [50], the Froude Number F_n is a dimensionless parameter measuring the ratio of the inertia force on an element of fluid to the weight of the fluid element. It is used to find the resistance coefficient c_R via the corresponding Harvald chart [47]

$$F_n = \frac{v}{(gL_{pp})^{1/2}} \quad (10)$$

From [22] and [52], the formula for the wetted surface area S is

$$S = 0.99 \left(\frac{\nabla}{T} + 0.19L_{wl}T \right). \quad (11)$$

Equation 12 [23] represents the ratio between volumetric displacement and the product of L_{wl} with the cross-sectional area of the submerged hull A_m [47].

$$C_p = \frac{\nabla}{(L_{wl}A_m)} \quad (12)$$

The air resistance coefficient [23] is determined by

$$c_{AA} = c_x \left(\frac{\rho_{air}A_x}{\rho_{seawater}S} \right), \quad (13)$$

where c_x is the air-drag coefficient of the vessel above the waterline, and 0.8 is usually used as the default value [49]. A_x is the projected area of the ship above the waterline.

The hydraulic roughness of the hull, also known as the roughness allowance coefficient, Δc_F is determined by [49]

$$\Delta c_F = 0.044 \left[\left(\frac{k_s}{L_{wl}} \right)^{1/3} - 10 \text{Re}^{-1/3} \right] + 0.000125, \quad (14)$$

where k_s indicates the roughness of the hull's surface, and the standard value of k_s is 150×10^{-6} [49].

Equation 15 [23] shows the effective power required to drag the ship through the water.

$$P_E = R_T v \quad (15)$$

However, we need to consider the efficiencies from the propellers η_o , transmission η_s , and hull η_H , and relative rotative efficiency η_R . Hence, Equation 16 shows the necessary power P_p , based on the efficiencies.

$$P_p = \frac{P_e}{\eta_T} = \frac{P_e}{(\eta_o \eta_s \eta_H \eta_R)} \quad (16)$$

For this thesis, the total efficiency η_T for this ship is assumed to be 70%. P_p is also often referred to as mechanical brake power P_B [52]. Based on Equations 3 to 16. Figures 9 and 10 show that as ship speed increases, the drag of the ship increases exponentially as along with the mechanical break power required to drive the ship forward.

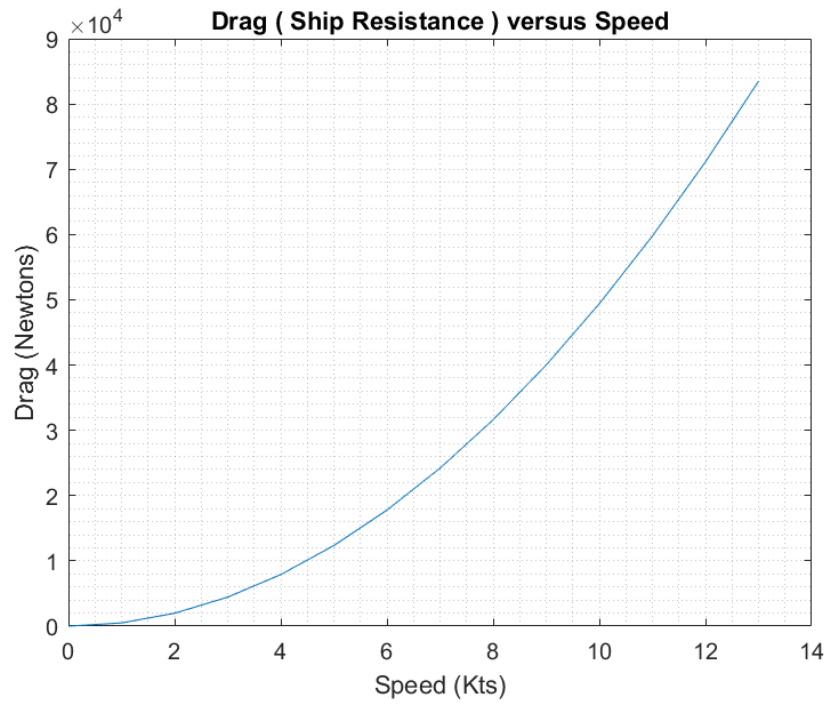


Figure 9. Drag versus speed graph.

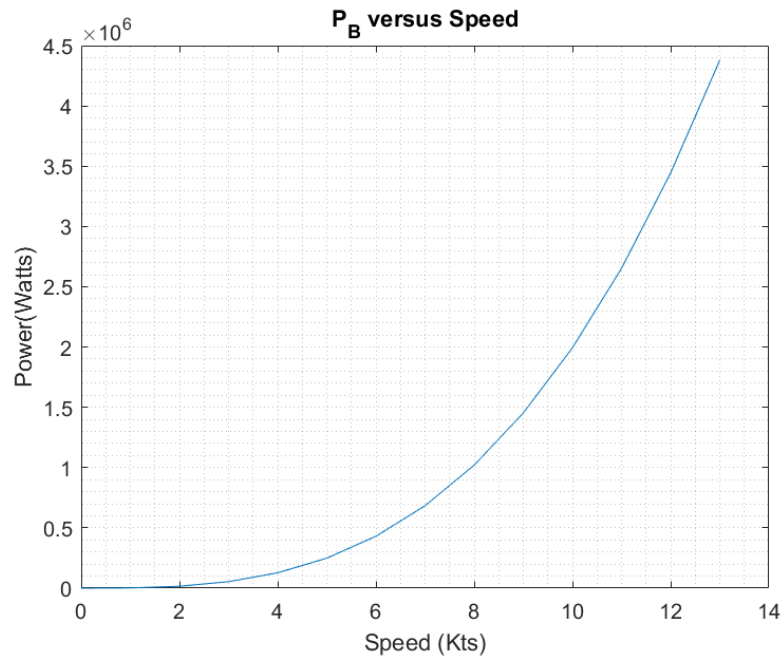


Figure 10. Brake power versus speed graph.

2. Ship Generators

The MF Oppedal ship is designed to travel up to 13 kts, and has four diesel engines aboard [23]:

- Two Mitsubishi GenSet S12RMPTA with 1100 kW each
- Two Mitsubishi GenSet S6R2MPTA with 640 kW each

B. LOAD MODEL

In our simulations the wave model simulates the load changes experienced by the ship sailing under various sea conditions. To simulate the wave action experienced by the ship, a sine wave was used to represent ship power demand. The sine wave would change in magnitude to simulate the changes in the sea condition from a light varying condition to a heavy varying condition as if the ship is sailing through a very severe sea state condition.

Although in this thesis we used only one stationary frequency component, the approach we present is general enough that it can be extended to more complex models with a number of frequency components that might even change with time.

As the sea conditions worsen, more power is required, and thus, a higher magnitude of the sine wave. Three wave profiles (15%, 25%, and 45%) are simulated for this paper. The first profile is a low-profile load simulating a small sea state. This implies that apart from the power P_B needed to keep forward motion at a constant velocity, an additional 15% of power is required to compensate for the effect of wave. The next profile is to simulate a moderate sea condition at 25% of the propulsion power and 45% for simulating heavy sea conditions.

The frequency of the profile depends on the wave, usually measured by when the two crests of a wave pass a point within a certain time frame. Adopted from a previous work [11], in our simulations we assume the wave period is 8 secs, which yields a fundamental frequency of 0.125Hz.

C. HYBRID ENERGY STORAGE SYSTEM

Based on the characteristics of the different energy storage devices shown in Figure 2, we can determine that no single device type can respond optimally to both high- and low-frequency power exchanges. The most common way to address this limitation is by combining multiple types of energy storage devices, thus forming the hybrid ESS (or HESS). A battery-SC combination is considered in most HESS developments because of the availability of these components, their similarity in working principle, their relatively low cost, and most importantly, the ability of each component to mitigate the limitations of the other component effectively. This combination is also commonly used for electrically-driven hybrid vehicles and residential energy storage microgrids and has been discussed extensively in much of the scholarly literature [30], [33], , [56]–[60].

Before establishing the battery-SC HESS size, we consider the specifications of the lithium-ion battery and supercapacitor, as shown in Tables 5 and 6.

Table 5. Specifications for lithium-ion battery. Source: [59].

Lithium-ion Battery	
Nominal Voltage	173V
Nominal Capacity	260AH
Energy	45kWh

Table 6. Specifications for SC. Source: [60].

125V Supercapacitor	
Rated Voltage	125V
Rated Capacitance	63F
Maximum Continuous Current	140A
Usable Specific Power	1,700 W [60]

The battery-SC HESS is sized according to the load generated by the highest wave profile of 45%. There can be many permutations for the HESS. The arrangement of the battery bank is designed to meet the power system requirements by adding batteries and SCs in a series to reach the desired direct current (DC) voltage.

D. HYBRID POWERTRAIN ARCHITECTURE

The powertrain of the hybrid ship considered in this thesis incorporates generators, batteries, and SCs. The total power required by the ship is split between the generators and the HESS. The generator will provide the steady current based on the desired speed, and the HESS will take up the varying current required due to the wave load profiles.

The power control presented in this thesis is based on a simplified dynamic model of the ship moving in the forward direction, propelled by its own power and subject to external forces such as drag and wave action. Its dynamics then can be written as

$$M\dot{v}(t) = F_{prop}(t) - F_{drag}(t) - \tilde{F}_{wave}(t), \quad (17)$$

where F_{prop} is the propulsion force, F_{drag} is the drag force, and \tilde{F}_{wave} is the force due to the wave. In steady state, the forward velocity is expressed as

$$v(t) = \bar{v} + \tilde{v}(t), \quad (18)$$

where \bar{v} is the steady state forward velocity and $\tilde{v}(t)$ is the velocity perturbation due to the wave. Then, expanding the drag resistance in a Taylor series around the steady state velocity \bar{v} , we obtain

$$M\dot{v}(t) = \bar{F}_{prop}(t) + \tilde{F}_{prop}(t) - F_{drag}(\bar{v}) - \nabla F_{drag}(\bar{v})\tilde{v}(t) - \tilde{F}_{wave}(t) \quad (19)$$

The following equation

$$\bar{P}_{prop} = \bar{F}_{prop} \bar{v} \quad (20)$$

is the power required to move the ship forward at the steady speed \bar{v} .

For the wave component, the propulsion power required to compensate for the wave action and keep the velocity perturbation $\tilde{v}(t)$ to a minimum is

$$\begin{aligned} \tilde{P}_{prop} &= \tilde{F}_{prop}(t)v \\ &\approx \tilde{F}_{prop}(t)\bar{v} \end{aligned} \quad (21)$$

Combining Equations 19–21, we obtain

$$\frac{\dot{\tilde{v}}(t)}{\bar{v}} = -\delta \frac{\dot{\tilde{v}}(t)}{\bar{v}} + \frac{1}{2(K)} (\tilde{P}_{prop}(t) - \tilde{P}_{wave}(t)), \quad (22)$$

where $\delta = \nabla F_{drag}(\bar{v}) / M$ and $K = \frac{1}{2} M \bar{v}^2$, where M is the mass of the ship.

Since the propulsion power comes from a number of energy sources, we can express that

$$\tilde{P}_{prop}(t) = \eta_{eff} (\tilde{P}_{gen}(t) + \tilde{P}_{batt}(t) + \tilde{P}_{SC}(t)) \quad (23)$$

with η_{eff} as the efficiency of energy conversion from electric to mechanical energy.

Assuming a constant bus voltage, we yield

$$\frac{\dot{\tilde{v}}(t)}{\bar{v}} = -\delta \frac{\dot{\tilde{v}}(t)}{\bar{v}} + \frac{V_{Bus}}{2(K)} \eta_{eff} (\tilde{I}_{gen}(t) + \tilde{I}_{batt}(t) + \tilde{I}_{SC}(t) - \tilde{I}_{wave}(t)) \quad (24)$$

with $\tilde{I}_{wave}(t)$ denoting the current required to fully compensate for the wave action on the forward velocity. Define

$$\tilde{x}_v(t) = \frac{2(K)}{V_{bus}} \frac{\tilde{v}(t)}{\eta_{eff} \bar{v}} \quad (25)$$

and Equation 24 becomes

$$\dot{\tilde{x}}_v(t) = -\delta \tilde{x}_v(t) + \tilde{I}_{gen}(t) + \tilde{I}_{batt}(t) + \tilde{I}_{SC}(t) - \tilde{I}_{wave}(t). \quad (26)$$

Expressing this equation in discrete time by approximating the derivative, we obtain

$$x_v(t+1) = (1 - \delta T_s) x_v(t) + \tilde{I}_{gen}(t) + \tilde{I}_{battery}(t) + \tilde{I}_{SC}(t) - \tilde{I}_{wave}(t), \quad (27)$$

where t is now the discrete time index and

$$x_v(t) = \frac{\tilde{x}_v(t)}{T_s} = \frac{2(K)}{V_{bus} T_s} \frac{\tilde{v}(t)}{\bar{v}}.$$

In these equations the bus voltage of the ship is 800V and assumed constant. If we define I_B as the steady state current to move the ship forward at a constant velocity \bar{v} the total current required is the sum of the wave current \tilde{I}_{wave} and the brake current I_B .

1. Diesel Generator Model

The diesel generator is also modeled in discrete time. The generator has two current components, I_B and \tilde{I}_{gen} . I_B provides a steady-state current based on the required power P_B necessary to keep the ship moving forward and maintaining its course. For this thesis, the goal of the MPC controller is to provide current, \tilde{I}_{gen} , for efficient use of the generator and energy storage sources in the presence of adverse sea conditions. Since it is desirable to keep the generator operating at a steady pace, avoiding deep swings in power, we define the state space model of the generator in terms of the current delivered \tilde{I}_{gen} , where ΔI_{gen} is the control variable, constrained to small rates of change:

$$\tilde{I}_{gen}(t+1) = \tilde{I}_{gen}(t) + \Delta I_{gen}(t). \quad (28)$$

2. HESS Model

The following section will elaborate on the state space equations for the battery and SC.

a. Battery

The main parameters of the battery are its capacity in Amps per hour (Ah) and State of Charge (SOC). The rated capacity is simply the energy capacity of the battery under normal conditions. For example, 200 Ah means if the battery is fully charged, in principle it could provide a sustained current of 200 Amps for one hour before it is completely discharged. The SOC reflects the level of charge of the battery relative to its capacity. The unit of SOC(t) is a percentage, and it indicates the amount of energy stored at time “t” versus the energy stored at rated capacity. There are also additional parameters defining battery performance such as the State of Health, State of Function, and shelf life. Those

factors will not be considered for this thesis. Mathematically, the battery state-space equations are defined in Equations 29 and 30.

$$\tilde{I}_{battery}(t+1) = \tilde{I}_{battery}(t) + \Delta I_{battery}(t) \quad (29)$$

$$SOC_{Batt}(t+1) = SOC_{Batt}(t) - \gamma \tilde{I}_{Batt}(t) \quad (30)$$

Adapted from [31], γ represents the charging and discharging factor of the battery. A positive current represents that the battery is providing current. The Coulomb counting method is used to determine γ , which can be defined as

$$\gamma = \frac{T_{wave}}{3600(Q)} \quad (31)$$

b. Supercapacitor

The fundamental properties for the SC are its voltage and capacitance, as the energy of a capacitor is defined as [61]:

$$E = \frac{1}{2} CV^2 \quad (32)$$

Similar to the battery, the SOC(t) of the SC has the same meaning as energy stored at time t versus energy stored at rated conditions. Mathematically, the state-space equation for the SC current and SOC are shown in Equations 33 and 34.

$$\tilde{I}_{SC}(t+1) = \tilde{I}_{SC}(t) + \Delta I_{SC}(t) \quad (33)$$

$$SOC_{SC}(t+1) = SOC_{SC}(t) - \beta \tilde{I}_{SC}(t), \quad (34)$$

where the β represents the charging and discharging factor for the SC. Adapted from [31], the value β can be defined as

$$\beta = \frac{T_{wave}}{C V_{max}} \quad (35)$$

c. State Space Model and Constraints

The state variables and inputs of the optimization problem are defined by

$$x(t) = \begin{bmatrix} x_v, \tilde{I}_{gen}, \tilde{I}_{battery}, SOC_{battery}, \tilde{I}_{SC}, SOC_{SC} \end{bmatrix}^T \quad (36)$$

and

$$u(t) = \begin{bmatrix} \Delta I_{gen}, \Delta I_{batt}, \Delta I_{sc} \end{bmatrix}^T. \quad (37)$$

In addition, we define the output of the system as $y(t) = \tilde{I}_{residual}(t)$, which represents the difference between the total current generated and the current required to fully compensate for the wave actions. This can be written as

$$\tilde{I}_{residual}(t) = \tilde{I}_{gen}(t) + \tilde{I}_{batt}(t) + \tilde{I}_{SC}(t) - \tilde{I}_{wave}(t). \quad (38)$$

Equations 27–30 and Equations 33–34 can be consolidated into a state-space matrix in the following form

$$x(t+1) = Fx(t) + Gu(t) + Bw(t) \quad (39)$$

$$\tilde{I}_{residual}(t) = Hx(t) + Ju(t) + Dw(t), \quad (40)$$

where

$$F = \begin{bmatrix} 1 & 1 & 1 & 0 & 1 & 0 \\ 0 & 1 & 0 & 0 & 0 & 0 \\ 0 & 0 & 1 & 0 & 0 & 0 \\ 0 & 0 & -\gamma & 1 & 0 & 0 \\ 0 & 0 & 0 & 0 & 1 & 0 \\ 0 & 0 & 0 & 0 & -\beta & 1 \end{bmatrix} \quad G = \begin{bmatrix} 0 & 0 & 0 \\ 1 & 0 & 0 \\ 0 & 1 & 0 \\ 0 & 0 & 0 \\ 0 & 0 & 1 \\ 0 & 0 & 0 \end{bmatrix} \quad B = \begin{bmatrix} -1 & 0 \\ 0 & 0 \\ 0 & 0 \\ 0 & 0 \\ 0 & 0 \\ 0 & 0 \end{bmatrix}$$

$$H = \begin{bmatrix} 0 & 1 & 1 & 0 & 1 & 0 \end{bmatrix} \quad J = \begin{bmatrix} 0 & 0 & 0 \end{bmatrix} \quad D = \begin{bmatrix} -1 & 0 \end{bmatrix}$$

At any time t , assuming we have full state observation $x(t)$, the goal of the controller is to find a sequence of predicted future inputs $u_{t|t}, u_{t|t+1|t}, \dots, u_{t+N|t}$, which minimizes the cost function

$$V(x(t), u_{t+k|t}) = \frac{1}{2} \sum_{k=0}^{N-1} \left(x_{t+k|t}^T Q x_{t+k|t} + u_{t+k|t}^T R u_{t+k|t} \right) + \left(x_{t|k}^T E u_{t|k} \right) + x_{t+N|t}^T P x_{t+N|t}, \quad (41)$$

where $x_{t+k|t}$ indicates the predicted state at time $t+k > t$ and $x_{t|t} = x(t)$ the current state. In this expression the rightmost term expresses the total cost from time $t+N$ to infinity, and the corresponding matrix P is computed from the Riccati equation associated with the Discrete Linear Quadratic Regulator.

In the application of this thesis, the parameters associated with the cost matrices Q and R are expressed in terms of the respective state variables as

$$V(x(t), u_{t:t+N}) = \frac{1}{2} \sum_k^{N-1} \left(q_{x_v} |x_v|_{t+k|t}^2 + q_{I_{gen}} |\tilde{I}_{gen}|_{t+k|t}^2 + q_{I_{batt}} |\tilde{I}_{batt}|_{t+k|t}^2 + q_{SOC_{batt}} |SOC_{batt}|_{t+k|t}^2 + q_{I_{sc}} |\tilde{I}_{sc}|_{t+k|t}^2 + q_{SOC_{sc}} |SOC_{sc}|_{t+k|t}^2 \right) \\ + \frac{1}{2} \sum_k^{N-1} \left(r_{gen} |\Delta I_{gen}|_{t+k|t}^2 + r_{batt} |\Delta I_{batt}|_{t+k|t}^2 + r_{sc} |\Delta I_{sc}|_{t+k|t}^2 \right) + \left(x(t)_{t+k|t}^T E^T J u(t)_{t+k|t} \right) + x_{t+N|t}^T P x_{t+N|t}. \quad (42)$$

The 'r' and 'q' subscripts denote the weighting factors on the states and input. Table 7 highlights each subscript and its function.

Table 7. Weightage factors on the states and input.

Subscript	Descriptions	
q_{xv}	Weightage on the x_v	The weightage determines how much emphasis is placed on the energy devices states; i.e., a higher factor weightage equates to a high penalty on the state. E.g., if q_{lbatt} is \gg than q_{lsc} , the SC will be utilized more than the battery.
$q_{I_{gen}}$	Weightage on the \tilde{I}_{gen}	
$q_{I_{batt}}$	Weightage on the \tilde{I}_{batt}	
$q_{SOCbatt}$	Weightage on the Battery SOC	
$q_{I_{sc}}$	Weightage on the \tilde{I}_{sc}	
q_{SOCsc}	Weightage on the SC SOC	This controls the rate of change for inputs.
r_{gen}	Weightage on the rate of change for ΔI_{gen}	
r_{batt}	Weightage on the rate of change for ΔI_{batt}	
r_{sc}	Weightage on the rate of change for ΔI_{sc}	

In order to better illustrate the specific implementation of the MPC, we follow an example where the time horizon has a length $N=3$ samples. Again, defining $t+k|t = t+k$, with $k \geq 0$ integer, the predicted time instant given the present time t , Equation 43 yields a simple recursion

$$x_{t+1|t} = Fx(t) + Gu(t) \quad (43)$$

$$x_{t+2|t} = Fx_{t+1|t} + Gu_{t+1|t} = F^2x(t) + FG u_{t+1|t} + Gu(t) \quad (44)$$

$$x_{t+3|t} = Fx_{t+2|t} + Gu_{t+2} = F^3x(t) + F^2Gu_{t+2|t} + FG u_{t+1|t} + Gu(t). \quad (45)$$

In this recursion, $x(t)$ indicates current state, which is observed, and $x_{t+k|t}, k > 0$ indicates predicted states, while $u_{t+k|t}$ for $k \geq 0$ denotes values of the inputs to be determined by optimization. In the MPC framework only $u(t) = u_{t|0}$ will be the actual input to the system.

The three preceding equations can be rewritten in block matrix form as

$$\begin{bmatrix} x(t) \\ x_{t+1|t} \\ x_{t+2|t} \\ x_{t+3|t} \end{bmatrix} = \begin{bmatrix} I \\ F \\ F^2 \\ F^3 \end{bmatrix} x(t) + \begin{bmatrix} 0 & 0 & 0 \\ G & 0 & 0 \\ FG & G & 0 \\ F^2G & FG & B \end{bmatrix} \begin{bmatrix} u(t) \\ u_{t+1|t} \\ u_{t+2|t} \end{bmatrix}$$

$$= S_x x(t) + S_u u_t$$

The terms in the cost function introduced in Equation 43 can then be written as a standard quadratic form as follows:

$$\sum_{k=0}^2 (x_{t+k|t}^T Q x_{t+k|t}) + (x_{t+3|t}^T P x_{t+3|t}) = \begin{bmatrix} x(t)^T & x_{t+1|t}^T & x_{t+2|t}^T & x_{t+3|t}^T \end{bmatrix} \begin{bmatrix} Q & 0 & 0 & 0 \\ 0 & Q & 0 & 0 \\ 0 & 0 & Q & 0 \\ 0 & 0 & 0 & P \end{bmatrix} \begin{bmatrix} x(t) \\ x_{t+1|t} \\ x_{t+2|t} \\ x_{t+3|t} \end{bmatrix}$$

$$= x^T(t) S_x^T \bar{Q} S_x x(t) + u_t^T S_u^T \bar{Q} S_u u_t + 2x^T(t) S_x^T \bar{Q} S_u u_t$$

while the other term of the cost function can be written as

$$\sum_{k=0}^{N-1} (u_{t+k|t}^T R u_{t+k|t}) = \begin{bmatrix} u_{t|t}^T & u_{t+1|t}^T & u_{t+2|t}^T \end{bmatrix} \begin{bmatrix} R & 0 & 0 \\ 0 & R & 0 \\ 0 & 0 & R \end{bmatrix} \begin{bmatrix} u_{t|t} \\ u_{t+1|t} \\ u_{t+2|t} \end{bmatrix} = u_t^T \bar{R} u_t$$

Putting everything together yields

$$V(x(t), u_t) = u_t^T \Gamma u_t + 2x(t)^T \Phi u_t + x(t)^T \Psi x(t), \quad (46)$$

where $\Gamma = S_u^T \bar{Q} S_u + \bar{R} + S_u^T \bar{E} + \bar{E}^T S_u$, $\Phi = S_x^T \bar{Q} S_u + \bar{S}_u^T \bar{E}$ and $\Psi = S_x^T \bar{Q} S_x$. This function is optimized with respect to the input vector u_t . The control input at time t then is the first element of the vector u_t , as $u(t) = u_{t|t}$.

d. Setup Constraints

The goal is to set up the minimization of the cost function $V(x(t), u(t))$ subject to the constraints that are based on the design consideration of the energy storage devices. Hence

$$-20A \leq x_v \leq 20A \quad (47)$$

$$-200A \leq \tilde{I}_{batt} \leq 200A \quad (48)$$

$$20\% \leq SoC_{batt} \leq 90\% \quad (49)$$

$$-240A \leq \tilde{I}_{SC} \leq 240A \quad (50)$$

$$10\% \leq SoC_{SC} \leq 90\% . \quad (51)$$

Compiling Equations 47 to 51 into the matrix form, we get

$$A_x x(k) \leq b_x \quad k = 1, \dots, N \quad (52)$$

$$A_u u(k) \leq b_u \quad k = 1, \dots, N . \quad (53)$$

For example, the constraints just defined for the battery current and SOC could be written in matrix form as

$$\begin{bmatrix} 1 & 0 \\ -1 & 0 \\ 0 & 1 \\ 0 & -1 \end{bmatrix} x(t) \leq \begin{bmatrix} 200 \\ 200 \\ 0.9 \\ -0.2 \end{bmatrix}$$

The aim of the optimization problem is to minimize the excursion of the generator current \tilde{I}_{gen} while compensating for wave action, subject to the constraints of the energy storage elements in terms of their currents $\tilde{I}_{batt}, \tilde{I}_{SC}$, and their states of charge. To this end,

we make use of the MATLAB function *mpcqp solvers*, which solves a quadratic programming problem in the form of Equation (42) with constraints using the KWIK algorithm [62].

e. Francis Equation

Since the model includes an external signal $w(t)$, which models the effects of wave on ship power, a particularly suitable approach is given by the use of the Francis Equation introduced in [63]. This approach is based on the fact that wave can be assumed as periodic, at least within a finite time interval, represented by sums of sinusoids. Consequently, they can be expressed in a state-space model which, in the case of one sinusoidal component, is of the form

$$w(t+1) = A_w w(t), \quad (54)$$

where

$$A_w = \begin{bmatrix} \cos \theta & -\sin \theta \\ \sin \theta & \cos \theta \end{bmatrix} \quad (55)$$

and θ being the digital frequency of the wave and the state $w(t) = [w_1, w_2]^T$. The wave act as an additional force that the ship has to overcome in addition to the drag, which was highlighted in Equation 39. It can be shown that steady state inputs and states solutions of the form

$$u(t) = Lw(t) \quad (56)$$

and

$$x(t) = Tw(t) \quad (57)$$

can be computed with L and T matrices of suitable dimensions (Figure 11).

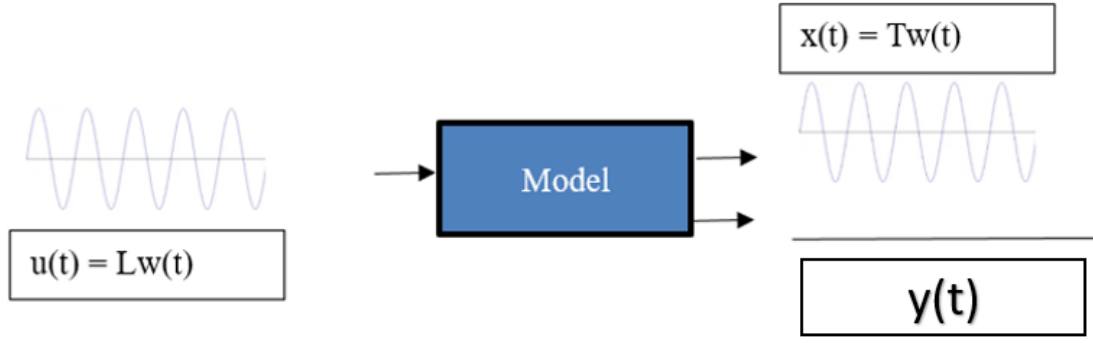


Figure 11. Illustration of the Francis equation.

The matrices T, L are solutions of the Francis equation defined as follows:

$$FT + GL + B = TA, \quad (58)$$

$$HT + JL + D = 0 \quad (59)$$

It is shown in [63] that a solution exists provided the matrices A and F have no common eigenvalues. Furthermore, based on the preceding definitions, we define new states $z(t)$ and input $v(t)$, respectively, as

$$z(t) = x(t) - Tw(t), \quad (60)$$

$$v(t) = u(t) - Lw(t). \quad (61)$$

Substituting Equations 61 and 62 into Equations 1 and 2, we obtain

$$z(t+1) = Fz(t) + v(t) \quad (62)$$

and

$$\tilde{I}_{res}(t) = Hz(t) + Jv(t). \quad (63)$$

The goal is to find a control input $v(t)$ for regulation of the system, so that the corresponding input $u(t) = v(t) + Lw(t)$ regulates the system.

Since the constraints stated in Equations 47 to 51 refer to the state and input vectors $x(t)$ and $u(t)$, we need to determine constraints in terms of $z(t)$ and $v(t)$. Recalling the constraints in $x(t)$ and $u(t)$ domain

$$A_x x(t) \leq b_x \quad (64)$$

and

$$A_u u(t) \leq b_u, \quad (65)$$

substituting Equations 64 and 65 into Equations 52 and 53, which yields

$$A_x z(t) \leq b_x - A_x T w(t) \quad (66)$$

and

$$A_u v(t) \leq b_u - A_u L w(t). \quad (67)$$

THIS PAGE INTENTIONALLY LEFT BLANK

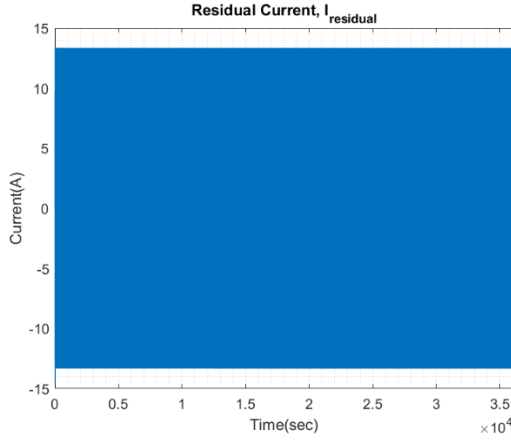
IV. RESULTS AND ANALYSIS

This chapter presents the results obtained after running several time-domain simulations of the model. No internal losses are assumed for the dynamics and they are assumed to be operating under ideal conditions. The aim of the model is to present the MPC algorithm and how it responds using different values of the weights in the cost function defined in Table 7. The model is implemented in MATLAB for three wave profiles. In particular, each scenario also compares the battery and SC current outputs based on different values of the weight q_{lbatt} in Table 7.

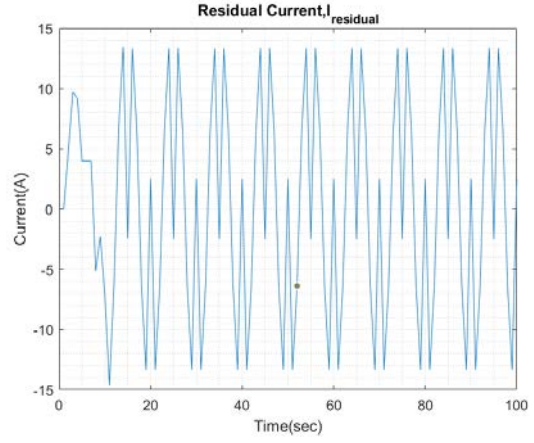
The MPC model illustrated in Chapter III is evaluated against six values of the weight q_{lbatt} (1, 5, 10, 20, 30, and 50). The objective is to keep the generator running at a steady state while the HESS is compensating for the wave when the ship is travelling at 11kts. The constraints stated in Equations 47–51 are also applied in the model. The simulation time for the model is 28,800 seconds, or 8 hours, so as to ensure the model is able to reach a steady-state output.

A. LIGHT SEA CONDITIONS (15% WAVE PROFILE)

In light sea conditions, the additional power required to navigate through the wave is approximately 390 kW, which is 15% of the power required to cruise in calm seas. The MPC model is able to optimize and minimize the generator current, \tilde{I}_{gen} , to a steady state of 108 A for all q_{lbatt} , while the battery and the SC are providing the rest of the required current to compensate for the wave action and keep the forward velocity of the ship as smooth as possible. Figure 12 shows the residual current, $\tilde{I}_{residual}$, at steady state and the expanded view of the initial transient response.



(a)



(b)

Figure 12. (a) $\tilde{I}_{residual}$ with q_{lbatt} and $q_{isc} = 1$. (b) Enhanced view of the $\tilde{I}_{residual}$ initial transient response.

Figure 13 shows the velocity perturbation $\tilde{v}(t)$. The model can reach steady state quickly and the velocity fluctuation is kept small. The goal is to keep the residual current $\tilde{I}_{residual}$ minimal. It is not possible, however, to minimize $\tilde{v}(t)$ and $\tilde{I}_{residual}$ to zero due to the constraints.

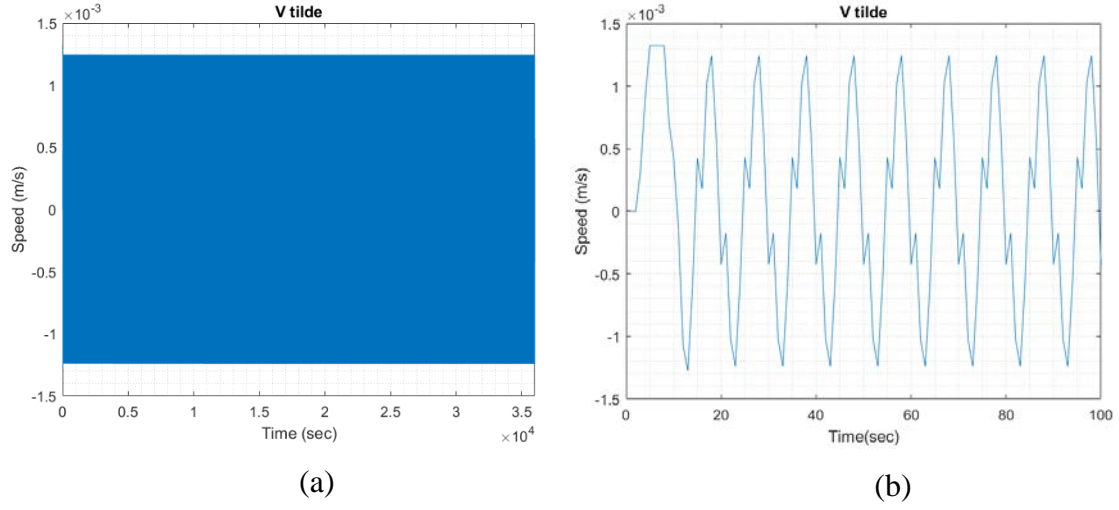


Figure 13. (a) $\tilde{v}(t)$ with q_{lbatt} and $q_{lsc} = 1$. (b) Enhanced view of the initial transient response.

As already observed, Figure 12 shows the plot for $\tilde{I}_{residual}$, where it can be noted that the transient response is small compared to the two other bigger wave profiles. The current $\tilde{I}_{residual}$ oscillates between ± 13 A at steady state for the rest of the simulation time.

Figure 14 shows the currents plots for \tilde{I}_{wave} , \tilde{I}_{gen} , \tilde{I}_{batt} , and \tilde{I}_{sc} . Figure 14(a) shows that the total current generated by \tilde{I}_{gen} , \tilde{I}_{batt} , and \tilde{I}_{sc} is able to compensate for \tilde{I}_{wave} and with the slight difference is as shown in Figure 12, while Figure 14(b) shows the individual current of \tilde{I}_{gen} , \tilde{I}_{batt} , and \tilde{I}_{sc} .

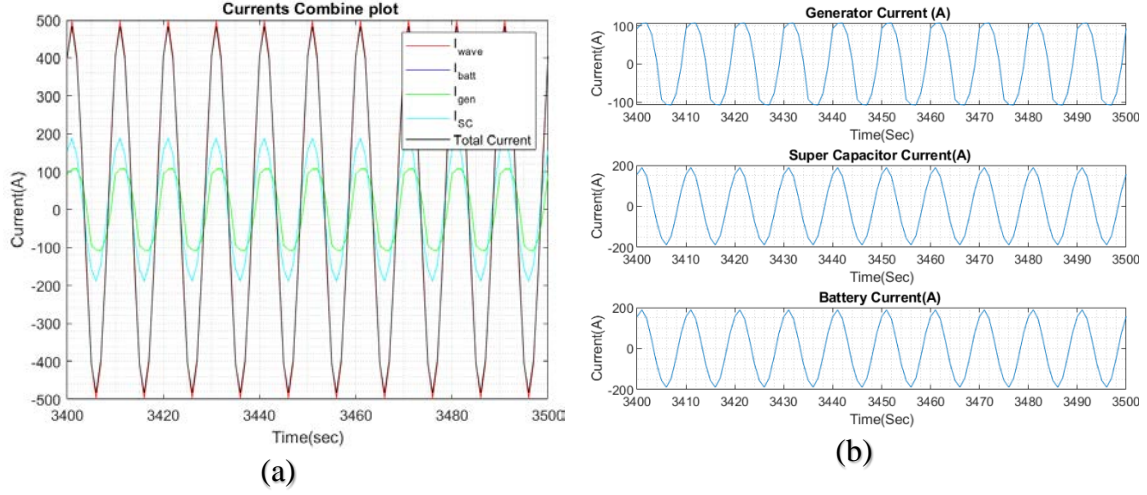


Figure 14. (a) Enhanced view of the \tilde{I}_{gen} , \tilde{I}_{batt} , and \tilde{I}_{sc} output currents with q_{lbatt} and $q_{Isc} = 1$. (b) A dissected view of the individual current.

As the value of weights q_{lbatt} and q_{Isc} are the same, the output currents from both devices are approximately the same. The slight difference is due to the different γ and β factors related to their SOC's. The rate of change for the generator ΔI_{gen} was set to 50 A per sample, corresponding to 62.5 Amps/sec to illustrate the slower rate of change as compared to the higher ΔI_{batt} , and ΔI_{sc} , and the difference is shown in Figures 14 and 16. As the \tilde{I}_{wave} is small, the rate of change for \tilde{I}_{gen} is not that significant and this observation can be seen in the higher wave profiles where the \tilde{I}_{wave} is larger. It is also observed that \tilde{I}_{gen} is slightly slower than the other two currents due to ΔI_{gen} .

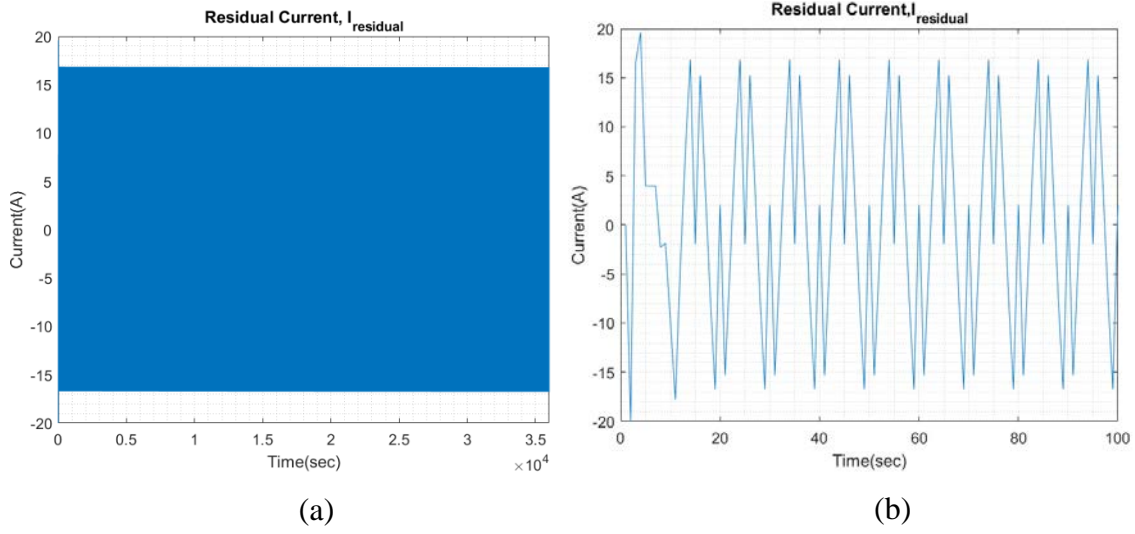


Figure 15. (a) $\tilde{I}_{residual}$ with $q_{Ibatt} = 30$ and $q_{Isc} = 1$. (b) Enhanced view $\tilde{I}_{residual}$ initial transient response

Figure 15 shows the $\tilde{I}_{residual}$ when q_{Ibatt} is increased to 30. It is observed that the transient response has a higher peak value although it has approximately the same settling time as Figure 12. The $\tilde{I}_{residual}$ can be further reduced by limiting the range of x_v . For this thesis, x_v is unchanged in order to observe the impact of q_{Ibatt} . $\tilde{I}_{residual}$ is able to reach steady-state and maintain at $\pm 16A$ throughout the simulation time.

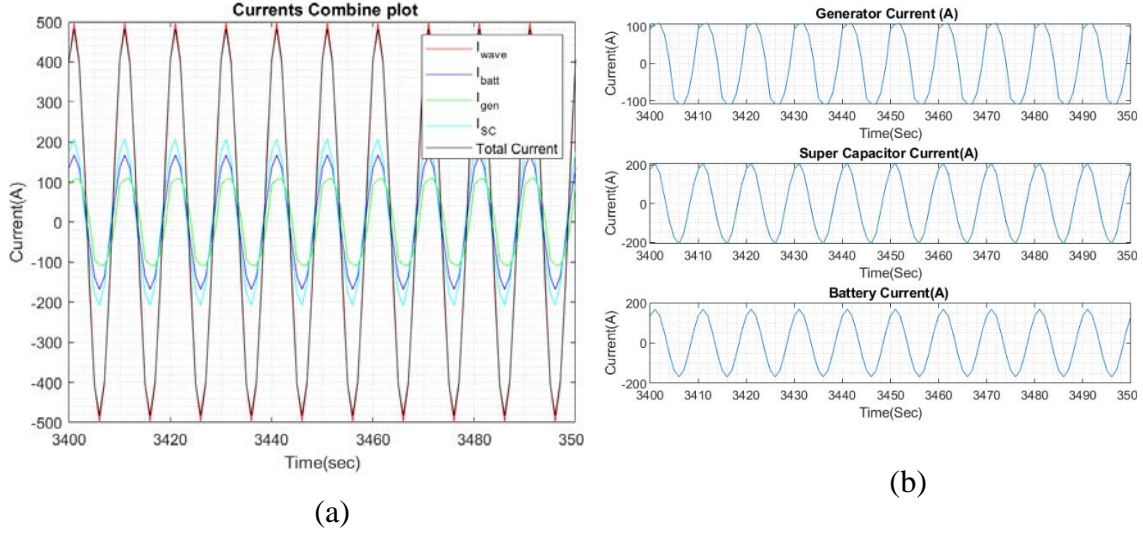


Figure 16. (a) Enhanced view of the \tilde{I}_{gen} , \tilde{I}_{batt} and \tilde{I}_{sc} output currents with $q_{lbatt} = 30$ and $q_{lsc} = 1$. (b) A dissected view of the individual current

Figure 16 shows the current plots for \tilde{I}_{wave} , \tilde{I}_{gen} , \tilde{I}_{batt} and \tilde{I}_{sc} . Figure 16(a) shows that the total current generated by \tilde{I}_{gen} , \tilde{I}_{batt} , and \tilde{I}_{sc} is able to compensate \tilde{I}_{wave} with the slight difference as shown in Figure 15, while Figure 16(b) shows the individual current of \tilde{I}_{gen} , \tilde{I}_{batt} , and \tilde{I}_{sc} . As the values of the weights increase, the difference in current between the battery and the SC increases, and as compiled in Table 8, the current differences start to taper off when q_{lbatt} is greater than 20.

Table 8 compares the values of the \tilde{I}_{gen} , \tilde{I}_{batt} , and \tilde{I}_{sc} peak output currents for the six different values of q_{lbatt} . As the \tilde{I}_{wave} is considered small, the difference between each q_{lbatt} is small. The difference would be more apparent as the wave profile increases. Nevertheless, it is observed that the \tilde{I}_{batt} decreases as q_{lbatt} increases. It is also observed that when q_{lbatt} is greater than 20, the difference between the battery and the SC starts to

taper off. Similar observations are seen for the larger wave profile. It is also noted that \tilde{I}_{gen} remained the same for all values for q_{lbatt} .

Table 8. Compilation of the peak output currents for \tilde{I}_{gen} , \tilde{I}_{batt} , and \tilde{I}_{sc} .

q_{lbatt}	\tilde{I}_{gen}	\tilde{I}_{batt}	\tilde{I}_{sc}
1	107.9A	188.63A	188.83A
5	107.9A	175.17A	200.8A
10	107.9A	171.23A	204.47A
20	107.9A	168.76A	206.79A
30	107.9A	167.84A	207.66A
50	107.9A	167.06A	208.39

B. MODERATE SEA CONDITIONS (25% WAVE PROFILE)

The moderate sea condition is commonly encountered by a ship during deployment, and wave amplitudes for this condition are slightly larger as compared to the light sea condition. Therefore, the ship is required to generate more power to compensate for the wave in order to maintain its velocity. The ship requires an additional 650 kW to navigate through the wave. For all values of q_{lbatt} , the MPC controller is able to optimize the states and minimize the generator peak output current \tilde{I}_{gen} to 163 A, while the battery and SC are providing the required currents to compensate for the wave. Similar to the light sea condition, $\tilde{v}(t)$ is observed to be small and this is consistent for all values of q_{lbatt} .

Figure 17 shows the velocity perturbation $\tilde{v}(t)$ during the moderate sea condition. As compared to the light sea condition, the model took a longer time to reach steady state, while the fluctuation is small. A similar observation is seen for all values of q_{lbatt} .

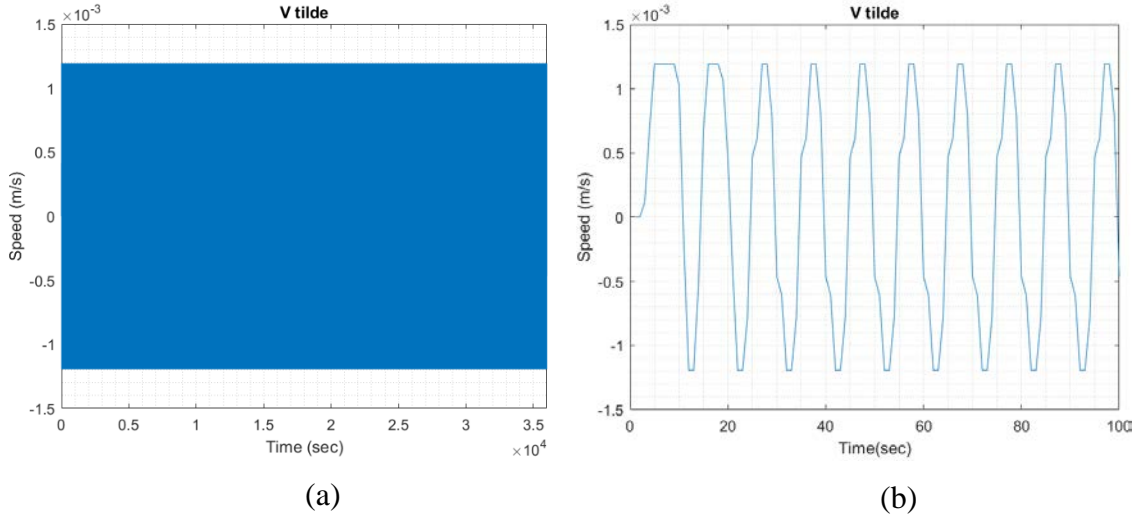


Figure 17. (a) $\tilde{v}(t)$ with q_{lbatt} and $q_{lsc} = 1$. (b) Enhanced view of the initial transient response.

Figure 18 shows the current difference $\tilde{I}_{residual}$ between the \tilde{I}_{wave} , \tilde{I}_{gen} , \tilde{I}_{batt} , and \tilde{I}_{sc} . Similar to Figure 17, the model took slightly longer to reach steady state as compared to light sea conditions. The steady state $\tilde{I}_{residual}$ is also slightly larger as compared to light sea conditions. This is expected as the required \tilde{I}_{wave} is larger. The $\tilde{I}_{residual}$ stabilized between $\pm 18A$ for the rest of the simulation time.

Figure 19 shows the currents plots for \tilde{I}_{wave} , \tilde{I}_{gen} , \tilde{I}_{batt} , and \tilde{I}_{sc} . Figure 19(a) shows that the total current generated by \tilde{I}_{gen} , \tilde{I}_{batt} , and \tilde{I}_{sc} is able to compensate for \tilde{I}_{wave} with the slight current difference is as shown in Figure 18. Figure 19(b) shows the individual current of \tilde{I}_{gen} , \tilde{I}_{batt} , and \tilde{I}_{sc} .

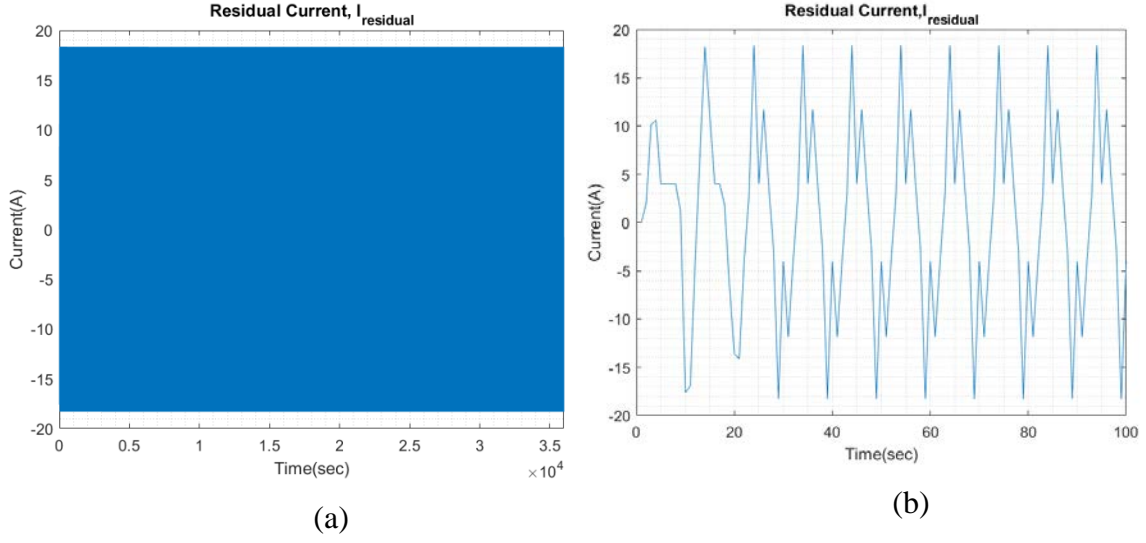


Figure 18. (a) $\tilde{I}_{residual}$ with q_{lbatt} and $q_{lsc} = 1$. (b) Enhanced view of $\tilde{I}_{residual}$ initial transient response.

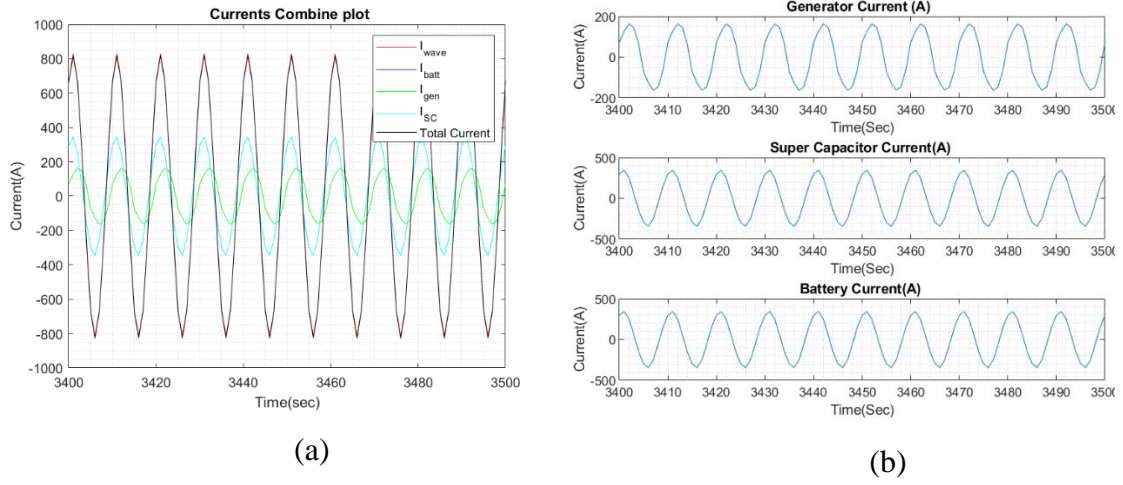


Figure 19. (a) Enhanced view of the \tilde{I}_{gen} , \tilde{I}_{batt} , and \tilde{I}_{sc} output currents with q_{lbatt} and $q_{lsc} = 1$. (b) A dissected view of the individual current.

As the value of the weights q_{lbatt} and q_{lsc} are the same, the output currents from both devices are approximately the same. The slight difference is due to the different γ and β factors. The rate of change for the generator ΔI_{gen} remains unchanged from the previous sea profile so as to illustrate the difference in rate of change as compared to the battery and the SC. As compared to light sea conditions, this is more evident in Figures 19 and 21 as \tilde{I}_{gen} waveform is observed to be slower than the rest of the current waveforms.

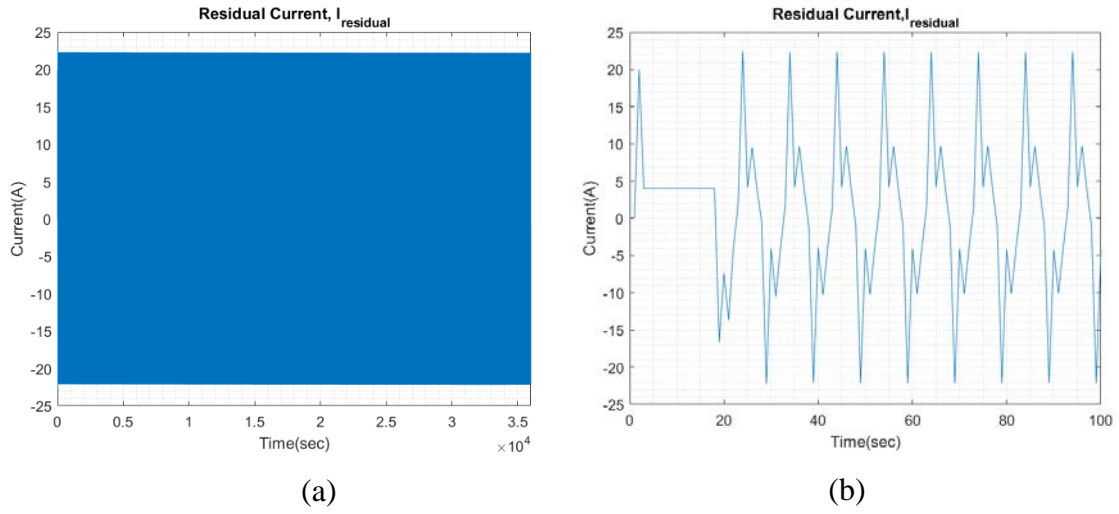


Figure 20. (a) $\tilde{I}_{residual}$ with $q_{lbatt} = 30$ and $q_{lsc} = 1$. (b) Enhanced view of the $\tilde{I}_{residual}$ initial transient response.

Figure 20 shows the plot of the $\tilde{I}_{residual}$ when q_{lbatt} is increased to 30. It is observed that the transient response is slightly longer than that shown in Figure 18 when q_{lbatt} is 1. This is because a higher penalty is put on the battery, thus reducing the battery output current at each sampling time. The $\tilde{I}_{residual}$ is able to maintain the steady-state oscillations between $\pm 22A$ throughout the simulation time.

Figure 21 shows the currents plots for \tilde{I}_{wave} , \tilde{I}_{gen} , \tilde{I}_{batt} , and \tilde{I}_{sc} when q_{lbatt} is increased to 30. Figure 21(a) shows that the total current generated by \tilde{I}_{gen} , \tilde{I}_{batt} , and \tilde{I}_{sc} is able to compensate \tilde{I}_{wave} with the slight current difference shown in Figure 20. Figure 21(b) shows the individual current of \tilde{I}_{gen} , \tilde{I}_{batt} , and \tilde{I}_{sc} .

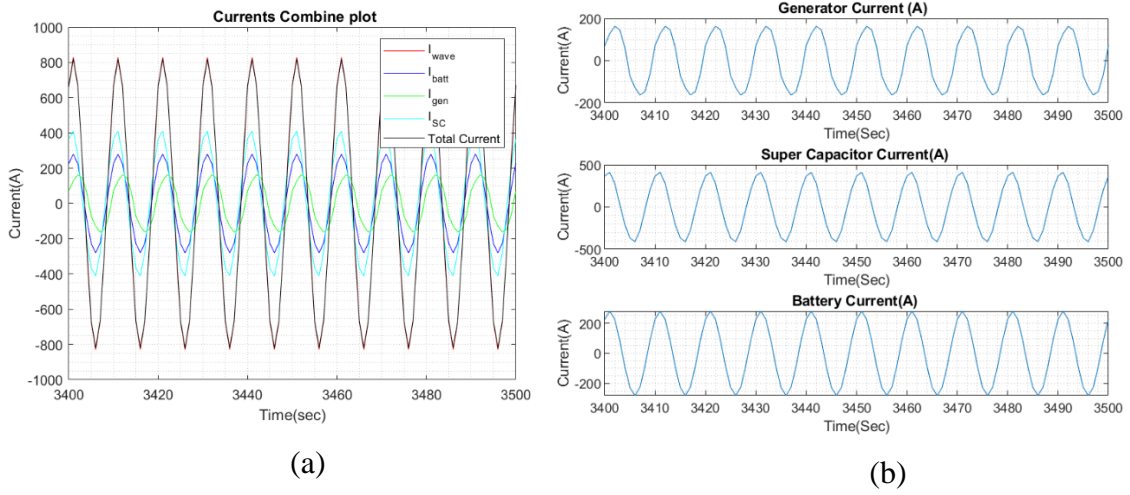


Figure 21. (a) Enhanced view of the \tilde{I}_{gen} , \tilde{I}_{batt} , and \tilde{I}_{sc} output currents with $q_{lbatt} = 30$ and $q_{lsc} = 1$.

As the value of the weight increases, the difference between the currents delivered by the battery and the SC, respectively, increases. Similar to the previous wave profile of 15%, the current differences start to taper off when q_{lbatt} is greater than 20. In comparison to the light wave conditions, the current differences for the q_{lbatt} in moderate sea conditions are larger. Table 9 compiles the steady-state peak output current for \tilde{I}_{gen} , \tilde{I}_{batt} , and \tilde{I}_{sc} based on different values of q_{lbatt} .

Table 9. Compilation of the peak output current for \tilde{I}_{gen} , \tilde{I}_{batt} , and \tilde{I}_{sc} .

q_{lbatt}	\tilde{I}_{gen}	\tilde{I}_{batt}	\tilde{I}_{sc}
1	163.17A	344.49A	345.01A
5	163.16A	305.60A	385.77A
10	163.15A	293.53A	397.98A
20	163.14A	285.78A	405.67A
30	163.14A	282.85A	408.54A
50	163.13A	280.36A	410.96A

In this simulation, \tilde{I}_{gen} remains at 163 A while the battery and SC are providing the required current to compensate for the effects of the wave expressed by \tilde{I}_{wave} . The difference in current between the battery and the SC is more substantial as q_{lbatt} increases. With the slower rate of change of the generator, the battery and SC is able to compensate the \tilde{I}_{wave} response effectively. This reduces the loading stress on the generator and reduces defective occurrences due to loading stress.

C. HEAVY SEA CONDITIONS (45% WAVE PROFILE)

The heavy sea condition is rarely encountered, and it represents a ship navigating through severe weather at sea. Under such a situation, without the ESDs, the generator will be placed under immense stress from generating the required fluctuating power when navigating up and down the wave. For this condition, the ship requires an additional 1.17 MW of power in order to compensate for the wave action and keep the forward velocity as steady as possible. As the demand is much higher, the rate of change ΔI_{gen} for this simulation also increases to 250 Amps/sec, indicating that more generators are operating to provide more power as well as to spread out the loading stress. After optimizing the

states and inputs by the MPC controller, the generator output current, \tilde{I}_{gen} , is maintained at 398 A, while the battery and the SC are generating the required currents to compensate for the wave. Similar to the previous two wave profiles, different q_{lbatt} weightages are analyzed.

Figure 22 shows the velocity perturbation $\tilde{v}(t)$ during the heavy sea condition. As compared to the previous two sea conditions, the model has a bigger initial transient response and $\tilde{v}(t)$ is larger. With the increased value of ΔI_{gen} , the model is able to reach steady state quickly. A similar observation can be made for all values of q_{lbatt} .

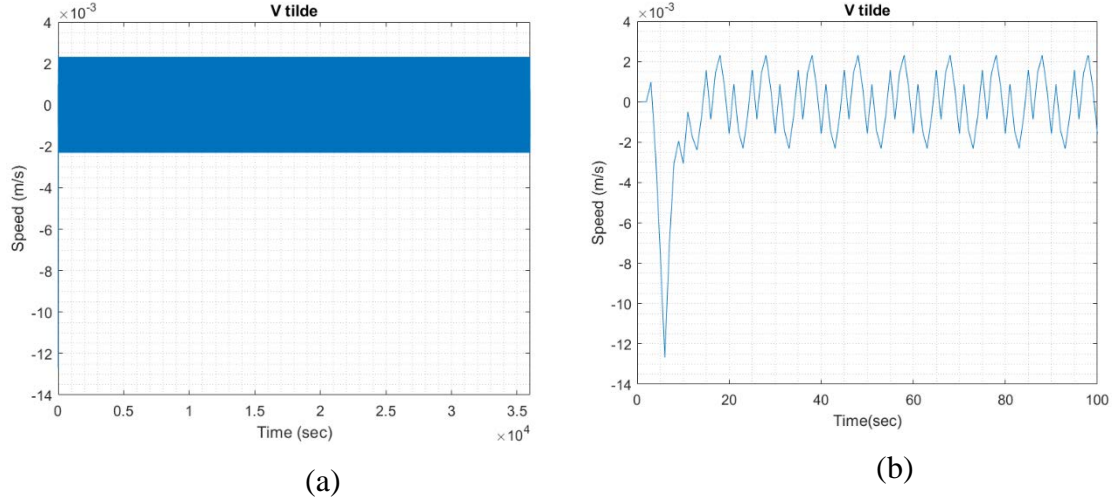


Figure 22. (a) $\tilde{v}(t)$ with q_{lbatt} and $q_{Isc} = 1$. (b) Enhanced view of the initial transient response.

Figure 23 shows the current $\tilde{I}_{residual}$, which is again the difference between the \tilde{I}_{wave} and the total generated current, which is the sum of \tilde{I}_{gen} , \tilde{I}_{batt} , and \tilde{I}_{sc} . The transient response has a higher peak value than the previous cases. The model is able to reach steady state quickly and is maintained at ± 30 A for the rest of the simulation time. Increasing the ΔI_{gen} will reduce the transient response and the steady state difference, but that would also indicate either more generators are connected to the ship microgrid or the generators are

taking on additional loading stress. An alternative is to select a battery and SC that have much larger capacity than the benchmark.

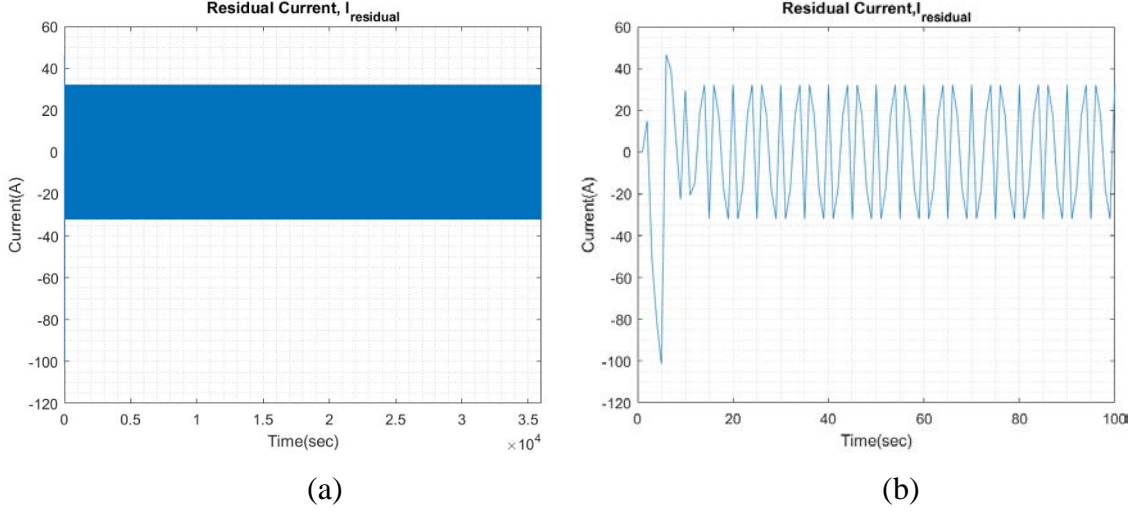


Figure 23. (a) $\tilde{I}_{residual}$ with q_{lbatt} and $q_{lsc} = 1$. (b) Enhanced view of $\tilde{I}_{residual}$ initial transient response

Figure 24 shows the currents plots for \tilde{I}_{wave} , \tilde{I}_{gen} , \tilde{I}_{batt} , and \tilde{I}_{sc} . Figure 24(a) shows that the total current generated by \tilde{I}_{gen} , \tilde{I}_{batt} , and \tilde{I}_{sc} is able to compensate for \tilde{I}_{wave} with the current differences as shown in Figure 23. Figure 24(b) shows the individual current of \tilde{I}_{gen} , \tilde{I}_{batt} , and \tilde{I}_{sc} . As the values of the weights increase, the difference between the battery and the SC increases as well. Similar to the previous two wave profiles, the current differences start to taper off when q_{lbatt} is greater than 20.

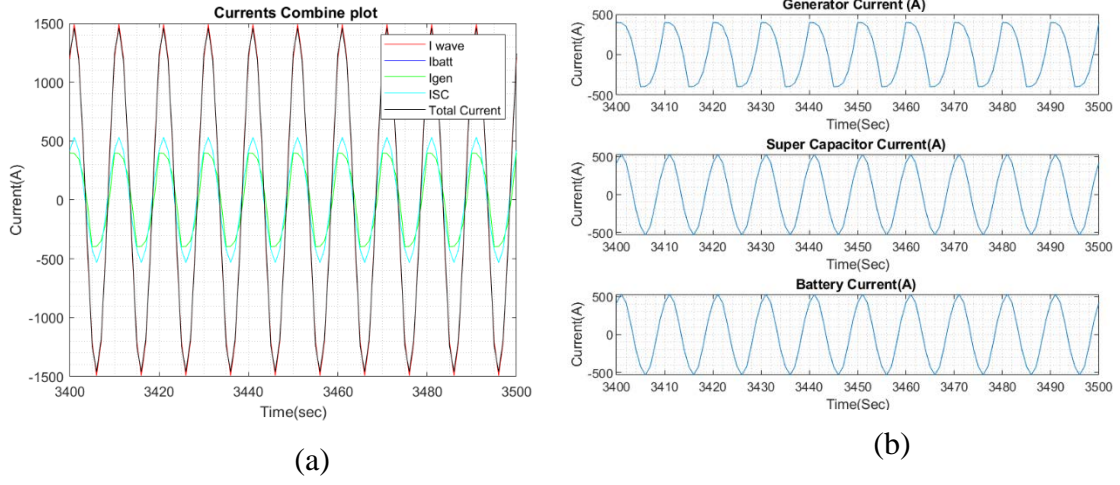


Figure 24. (a) Enhanced view of the \tilde{I}_{gen} , \tilde{I}_{batt} , and \tilde{I}_{SC} output currents with q_{Ibatt} and $q_{Isc} = 1$. (b) A dissected view of the individual current.

Figure 25 shows the $\tilde{I}_{residual}$ when q_{Ibatt} is increased to 30. It is observed that the transient response is much larger when q_{Ibatt} is 1, as shown in Figure 23. The $\tilde{I}_{residual}$ is able to reach steady state and maintain oscillations of $\pm 42A$ throughout the simulation time.

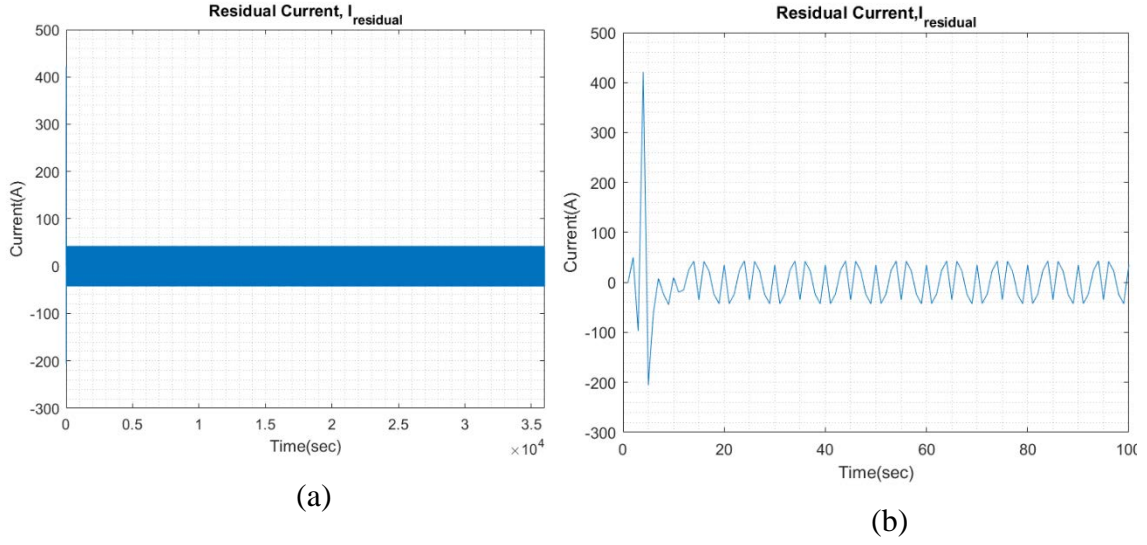


Figure 25. (a) $\tilde{I}_{residual}$ with $q_{lbatt} = 30$ and $q_{lsc} = 1$. (b) Enhanced view of $\tilde{I}_{residual}$ initial transient response

Figure 26 shows the currents plots for \tilde{I}_{wave} , \tilde{I}_{gen} , \tilde{I}_{batt} , and \tilde{I}_{sc} when q_{lbatt} is increased to 30. Similar to the previous two wave profiles, as the weightages increase the difference between the battery and the SC increases. The current difference between the battery and the SC, respectively, starts to taper when q_{lbatt} is greater than 20, while the \tilde{I}_{gen} is maintained at 398A. With a higher ΔI_{gen} , the ESDs are still able to generate most of the required current in order to compensate for the wave current.

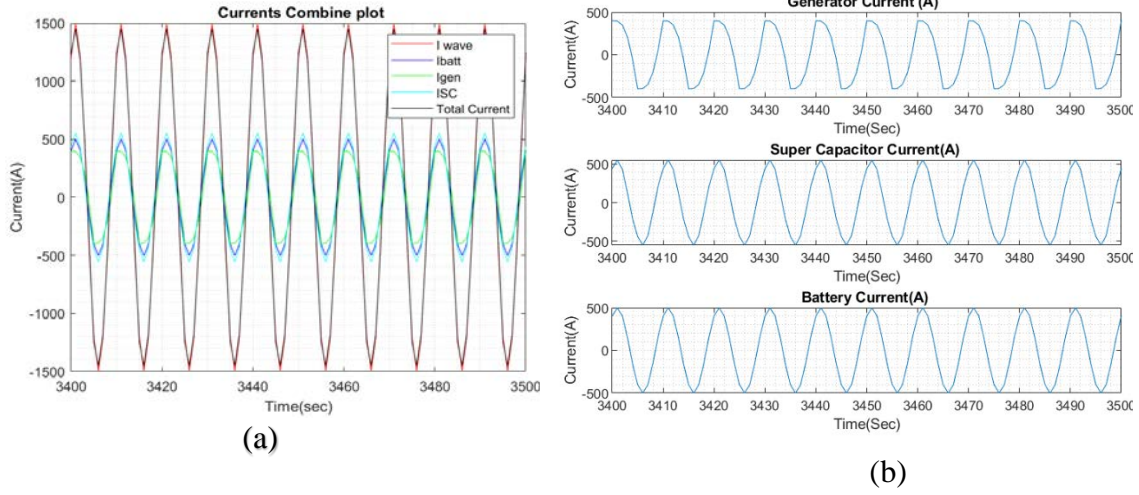


Figure 26. (a) \tilde{I}_{gen} , \tilde{I}_{batt} and \tilde{I}_{sc} output currents with $q_{lbatt} = 30$ and $q_{isc} = 1$.
(b) A dissected view of the individual current

Table 10 shows the steady-state peak output current for the \tilde{I}_{gen} , \tilde{I}_{batt} , and \tilde{I}_{sc} based on different q_{lbatt} weightages. The difference between the currents is not as substantial it was for the moderate sea condition due to the increased ΔI_{gen} .

Table 10. Compilation of the peak output current for \tilde{I}_{gen} , \tilde{I}_{batt} , and \tilde{I}_{sc} .

q_{lbatt}	\tilde{I}_{gen}	\tilde{I}_{batt}	\tilde{I}_{sc}
1	398.20A	532.48A	532.79A
5	398.46A	511.89A	546.47A
10	398.50A	505.91A	550.18A
20	398.52A	502.13A	553.13A
30	398.53A	500.70A	554.31A
50	398.52A	499.45A	555.32A

One common observation for all three wave profiles is that the battery and the SC output currents begin to taper off when q_{lbatt} is greater than 20. This highlights that an increase in the difference between the states greater than 20 does not have a significant impact for this model. The ESDs are able to compensate for most of the \tilde{I}_{wave} , thus reducing the stress on the generator significantly.

D. ESD STATE OF CHARGE

Figures 27 and Figures 29 compare the battery and the SC SoC at two different values of the weight q_{lbatt} ($q_{lbatt} = 1$ and $q_{lbatt} = 30$), respectively, using the moderate wave profile as this is the scenario most commonly encountered during sailing. It is observed that the SC SOC reaches its maximum rated value of 90% more quickly at a lower q_{lbatt} as compared to a higher q_{lbatt} weightage. This is expected as both ESDs are providing approximately the same amount of current, and when the SC has reached its rated capacity, the additional current during the charging phase is diverted to charge the battery. This is evident as the battery SOC starts to increase when the SC SOC has reached its upper limit set in Equation (51). As q_{lbatt} increases, the SC is providing more current as compared to the battery. The SC SOC requires more time before reaching its maximum rated SOC and before the additional current is diverted to charge the battery.

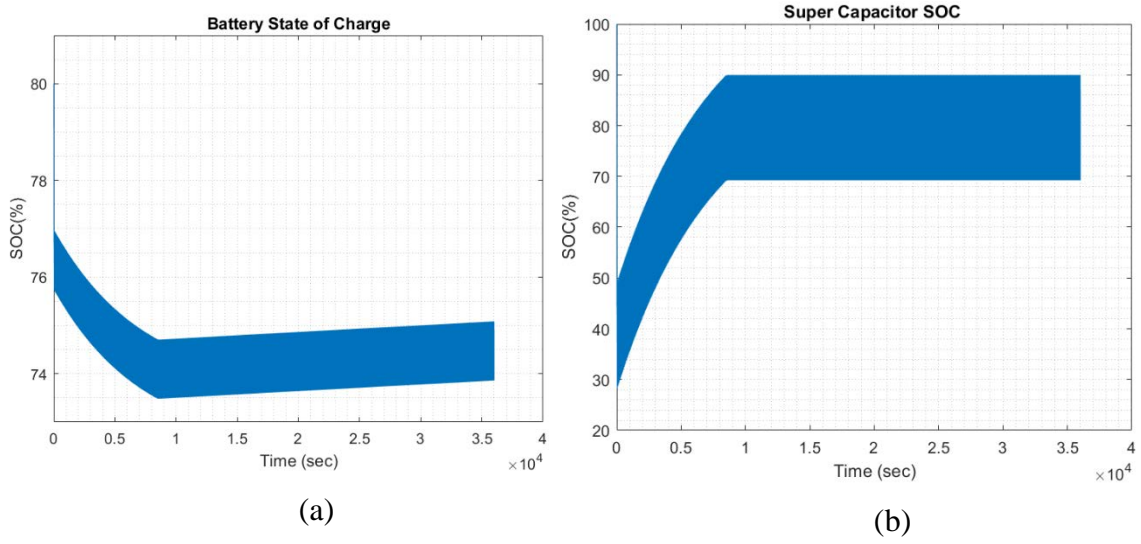


Figure 27. (a) Battery SoC. (b) SC's SoC when $q_{lbatt} = 1$.

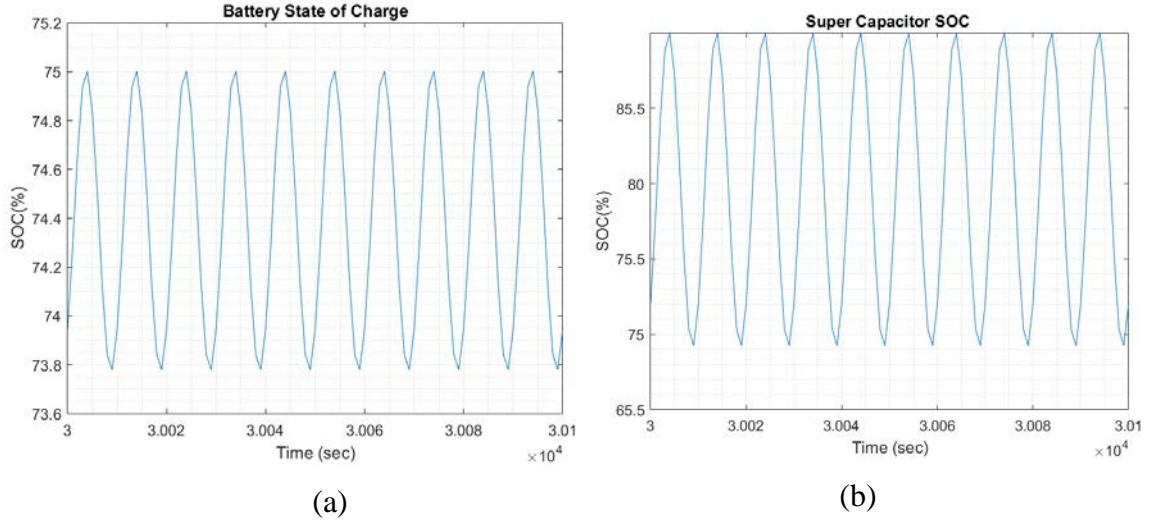
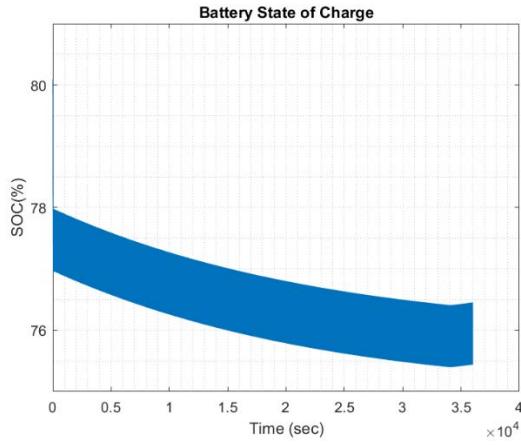
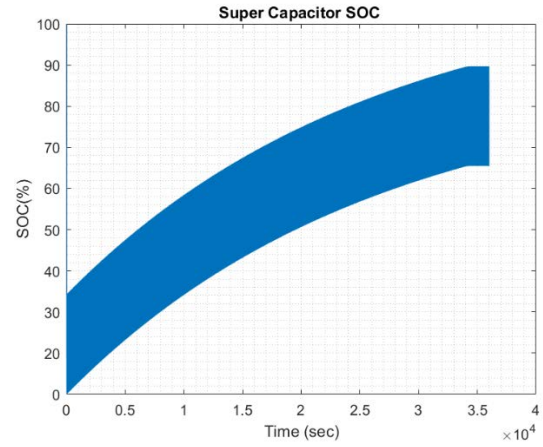


Figure 28. Enhanced views of (a) Battery SoC (b) SC SoC when $q_{lbatt} = 1$.

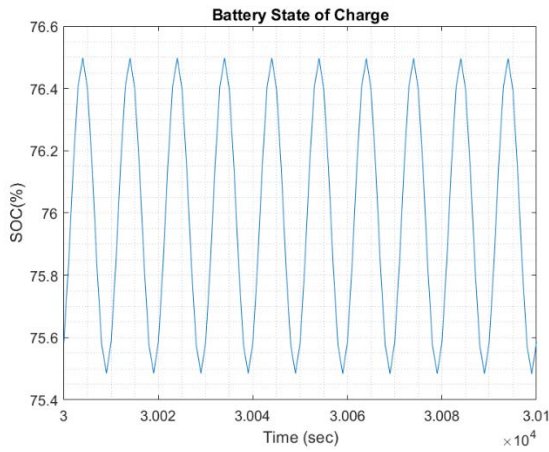


(a)

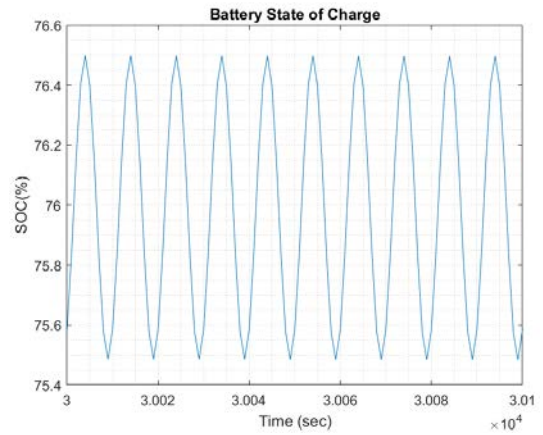


(b)

Figure 29. (a) Battery SoC (b) SC SoC when $q_{lbatt} = 30$.



(a)



(b)

Figure 30. Enhanced views of (a) Battery SOC (b) SC SOC when $q_{lbatt} = 30$.

V. CONCLUSION AND RECOMMENDATIONS FOR FUTURE WORK

This chapter presents the conclusion based on the results of the model developed and tested in this thesis. Areas for future work are also recommended, including implementing the model for different kinds of ships, designing a Kalman filter to estimate the state of the dynamic model for the wave action, having different charging and discharging factors for the battery and SC, and simulating a more realistic wave model.

A. CONCLUSION

In this thesis, we presented a control system that uses a combination of power generation and energy storage to keep a ship on a steady pace in different sea conditions. Although the work is preliminary and based on ideal, simplified conditions, it shows that a control system that uses the Francis Equation [63] to model periodic perturbations, and Model Predictive Control (MPC) to include physical limitations, can be a viable solution to this problem.

In particular, it shows that the integration of ESDs in the ship microgrid provides numerous advantages, such as increasing fuel efficiency, reducing loading stress on the generator, ensuring stability in the overall powertrain, and providing cost benefits due to improved generator maintenance. Moreover, it also helps provide environmental benefits as the generators are operating at steady-state speed with the aid of the ESDs.

A model of this sort could also be developed as a useful tool that enables the designer to size ESDs, such as batteries and supercapacitors, for practical applications. This conclusion is based on the fact that, at each iteration, the MPC controller searches for an optimal solution based on physical constraints of the various devices. If the components are not properly sized (for instance, inadequate storage devices) the controller fails to find a solution, which is remedied by properly increasing storage capacities.

B. FUTURE WORK

This research serves as a preliminary study into how MPC is an effective energy control management tool for a ship microgrid and further expansions can be implemented to improve its robustness.

There are several areas of follow-on research that can be pursued from this thesis. One area to explore is to design a Kalman filter to track a varying load profile. For example, the ship is navigating at low speed when exiting and entering ports and increasing to cruising speed through the open sea. Also, other electrical loads could be considered in the simulation. Such simulations might include higher power machineries such as bow thrusters operating during docking and weapons systems such as the U.S. Navy electromagnetic rail gun. Further, the model could be expanded to other sizes of ships.

Additional studies could explore different charging and discharge gammas and betas for the battery and supercapacitor. Such investigations would improve the model in modeling the characteristics of the devices.

Similarly, the wave model could be expanded to be more realistic. The current wave model only represents two-dimensional wave, and that could be extended to more complex models with a number of frequency components with might even change with time.

Lastly, this preliminary study of the MPC algorithm on a HESS could be expanded to model a land-based microgrid or forward-operating grid with more than one energy source.

APPENDIX. MATLAB SCRIPT

A. MAIN SCRIPT

```
% MF Oppedal
%
%

v_kn =11 % Enter desired speed

[Pe,v,DSP] = shippower(v_kn);

v % speed in meters per seconds
DSP % mass of ship, kg
Pp = Pe *4 % 4 Engines total requirement
Vbus = 800;
I_bus = Pp/Vbus % total current required move
forward without the current effect, FB-Fdrag
%% MPC Control

% Ship Generator Parameters
Pgwer = 2*(1.1e6) ; % MW
IGeny = Pgwer / Vbus

% Battery
Voc =12'
Q_batt = 200 ; % AH, capacity of battery;

%SuperCapacitor
% 125V module_datasheet_maxwell 125V heavy
transportation module SC
Cap_number = 7; % 800V/136 = 6 cap
Vmax = 135; % SuperCapacitor Vmax , Vrated =
125V
SC_Cap = 63; % SC capacitance

%wave parameters
```

```

F_wave = 0.125 ; %Hz
T_wave = 1 / F_wave ; % 8 Secs
FS = F_wave*10 % sampling frequency %
Ts = 1/FS
random_number = rand*randi([0 2]) * pi; %
alpha =0%random_number %0.5204
theta0 = 2*pi*(F_wave/FS)

%%Setting simulation time
T_final = 1* 3600 % 1 hour

N_final= T_final*FS ;

t = 0:N_final-1; % setting the intergers based
on simulation time

% %Variation in load from load profile %
SS_factor = 0.25 ;% 15% 25% and 45%

I_wave = (SS_factor*I_bus) * (cos(theta0*t +
alpha)); %Iwave based on load profile %Change
term
I_Overall = I_bus+I_wave;

max(I_wave);
min(I_wave);

Amplitude = 0.5* (max(I_wave) -
min(I_wave))%load_var; % amplitude of the wave
curve

%Getting amplitude of the waves , w1 and w2

w1 = Amplitude * cos(alpha) % Iwave based on w1
w2 = Amplitude * sin(alpha) % Iwave based on w2
%%

```

```

[e,x,u,w]=Powerscript(I_wave,w1,w2,theta0,FS,IG
eny,t,Voc,Q_batt,Vmax,SC_Cap,T_wave);

%%
% V_tilde_dot / V_bar

eff = 0.9;
K= 1/2 *DSP*(v^2)

V_tilde_dot_V_bar = (Vbus / (2*K) )* Ts *eff
*x(1,:);

V_tilde = ((Vbus / (2*K) )* Ts *eff *x(1,:) * v
);

figure(49)
plot(V_tilde)
title("V tilde")
xlabel("Time (sec)")
ylabel("Speed (m/s)")
xlim([0 length(t)])

figure(40)
plot(V_tilde)
title("V tilde")
xlabel("Time(sec)")
ylabel("Speed (m/s)")
xlim([0 100])
%%
set(groot,'defaultAxesXMinorGrid','on','default
AxesXMinorGridMode','manual');
set(groot,'defaultAxesYMinorGrid','on','default
AxesYMinorGridMode','manual');

XV = x(1,:);
Igen = x(2,:);
Ibatt= x(3,:);

```

```

SOC_Batt = x(4,:);
ISC= x(5,:);
SOC_UC = x(6,:);

x_T = transpose(x); % use for compiling

%%U(t)

Delta_Igen = u(1,:);
Delta_Ibatt = u(2,:);
Delta_ISC = u(3,:);

%outputvy(t)
figure(1)
plot(e); % y(t)
title('Residual Current, I_{residual}')
xlabel("Time(sec)")
ylabel("Current(A)")
xlim([0 length(t)])

figure(41)
plot(e); % y(t)
title(['Residual Current,I_{residual}'])
xlabel("Time(sec)")
ylabel("Current(A)")
xlim([0 100])

% Battery Output graphs
figure(2)
subplot(2,1,1)
plot(Ibatt)
title ("Battery Current (A)")
xlabel("Time (sec)")
ylabel ("Current (A)")

subplot(2,1,2)

plot(SOC_Batt)

```

```

title ("Battery State of Charge")
xlabel("Time (sec)")
ylabel ("SOC(%)")

figure(50)
% % invert the graph
SOC_Batt_Inv = SOC_Batt*-1;
plot(SOC_Batt_Inv)
title ("Battery State of Charge")
xlabel("Time (sec)")
ylabel ("SOC(%)")

yticks([ -0.08 -0.06 -0.04 -0.02 0])
yticklabels({'72','74','76','78','80'}) % set
the label to percentage

% % invert the graph , enhance view
SOC_Batt_Inv = SOC_Batt*-1;
plot(SOC_Batt_Inv)
title ("Battery State of Charge")
xlabel("Time (sec)")
ylabel ("SOC(%)")
xlim([30000 30100])

yticks([ -0.046 -0.044 -0.042 -0.04 -0.038 -
0.036 -0.034])
yticklabels({'75.4','75.6','75.8','76','76.2','
76.4','76.6'}) % set the label to percentage

%%%Generator output graphs
figure (3)
plot(Igen)

title("Generator Current ")
xlabel("Time (sec)")
ylabel ("Current (A)")

```

```

%%%Super Capacitor plotting
figure(4)
subplot(2,1,1)
plot(ISC)
title("Super Capacitor Current(A) ")
xlabel("Time (sec)")
ylabel ("Current (A)")

subplot(2,1,2)

plot(SOC_UC)

title("Super Capacitor SOC ")
xlabel("Time (sec)")
ylabel ("SOC(%)")

figure(55)

SOC_UC_Inv = SOC_UC*-1; % inverse the plot
plot(SOC_UC_Inv)
%
yticks([-0.9 -0.8 -0.7 -0.6 -0.5 -0.4 -0.3 -0.2
-0.1 0])
yticklabels({'0','20','30','40','50','60','70',
'80','90','100'}) % set the label to percentage
title("Super Capacitor SOC ")
xlabel("Time (sec)")
ylabel ("SOC(%)")

% % invert the graph , enhance view
SOC_UC_Inv = SOC_UC*-1; % inverse the plot
plot(SOC_UC_Inv)
title("Super Capacitor SOC ")
xlabel("Time (sec)")
ylabel ("SOC(%)")
xlim([30000 30100])

```

```

yticks([-0.35 -0.3 -0.25 -0.2 -0.15 -0.1])
yticklabels({'65.5','75','75.5','80','85.5','90'
'}) % set the label to percentage

title("Super Capacitor SOC ")
xlabel("Time (sec)")
ylabel ("SOC(%)")


% % %
%% Comparison

%%ISC and IBatt
figure(5)
plot(ISC)
hold on
plot(Ibatt)
hold off
legend("Isc","Ibattt")
title("Ibatt and ISC")
xlabel("Time(sec)")
ylabel("Current(A)")

%%% Current comparisons
figure(7)
plot(w(1,:), "r") % wave curent
hold on
plot(Ibatt, "b") %battery current
plot(Igen, "g") %Generator current
plot( ISC, "c") % SC current
plot(Igen+(Ibatt)+(ISC), "k") % total current
legend("I wave", "Ibatt", "Igen", "ISC", "Total
Current")
title(" Currents Combine plot")
hold off
xlabel("Time(sec)")

```

```

ylabel("Current(A) ")

figure(30)
plot(w(1,:), "r")
hold on
plot(Ibatt, "b")
plot(Igen , "g")
plot( ISC, "c")
plot(Igen+(Ibatt)+(ISC), "k")
xlim([3400 3500])
legend("I_{wave}", "I_{batt}", "I_{gen}", "I_{SC}"
, "Total Current")
title(" Currents Combine plot")

xlabel("Time(sec) ")
ylabel("Current(A) ")
hold off

figure(31)
subplot(3,1,1)
plot(Igen)

title("Generator Current (A) ")
xlabel("Time(Sec) ")
ylabel("Current(A) ")
%ylim([-250 250])
xlim([3400 3500])

subplot(3,1,2)
plot(ISC)
title("Super Capacitor Current(A) ")
xlabel("Time(Sec) ")
ylabel("Current(A) ")
%ylim([-250 250])
xlim([3400 3500])

subplot(3,1,3)

```

```

plot(Ibatt)
title("Battery Current(A) ")
xlabel("Time(Sec)")
ylabel("Current(A)")
ylim([-250 250])

xlim([3400 3500])

Geny_max = max((Igen(3400:3500)))
Batt_max = max((Ibatt(3400:3500)))
SC_max = max((ISC(3400:3500)))
hold off

```

B. SHIPPOWER FUNCTION

```

function [Pe,v,DSP] = shippower(v_kn)
% % MF Oppedal
% %
% % numbers of the battery, add SC and
simulink,

% Drag calculation for MF Oppedal

%Standard Parameters

rho_h2o = 1025; %kg/m^3 density of seawater
rho_air = 1.22; %kg/m^3 desity of air
g = 9.81; %ms^-2
vis = 1.15*10^-6; %ITTC Fresh Water and
Seawater Properties avg viscosity (kin.
vis./rho)

% v_kn = 15; %linspace(1,15,30);
v = v_kn * 0.514444; %conv. to ms^-1

%Dimensions in m
B = 16 ; %breadth

```

```

Lpp = 105 ; %m perpendicular length source:
Kullmann
LWL = Lpp * 0.97 ; % 97% of Lpp, according to
literature
DSP = 1705*10^3 ; % kg Displacement (weight)
PLD = 600*10^3 ; %kg payload max.
nabla = (DSP+PLD)/rho_h2o ; % Displacement
volume on maximum cap.
A_m = 18*2.3 ; % assumed wetted cross section
area
T = 3.3 ; % m from www.marinetraffic.com
(average value)
A_x = 18*10 ; % assumed cross section area
above water
Re = (5e8)/(v * LWL)/vis % Reynold No.
Fn = v/((g*Lpp)^0.5) ; %Froude number
S = 0.99 * ((nabla/T)+1.9*LWL*T) ;% wetted
surface area Mumford

% %%%RESISTANCE COEFFICIENTS%%%

C_B = nabla / (LWL*B*T); % block coeff
C_F = 0.075 / ((log10(Re) - 2 )^2);
;%frictional Resistance
C_X = 0.8; % for bulky geometries --> acc. to
ITTC
C_AA= C_X * ((rho_air*A_x)/(rho_h2o*S)); % air
Res.
C_P = nabla/(LWL*A_m); %prismatic coefficient
% residual coeff.
C_R = 1*10^-4;%from Harvald/Guldhammer Chart

% Form Factor k
k = -0.095 + 25.6 * (C_B/(LWL/B)^2 * (B/T)^0.5);
%Length Displ. Ratio
LDR = Lpp/(nabla^(1/3)); %molto importante to
determine which diagram to use

```

```

C_RA = 0.044 * (((((150*10^-6)/LWL)^(1/3)) -
10*(Re^(-1/3))))+0.000125; % roughness allowance
%TOTAL COEFF
C_T = (1+k)*C_F + C_R + C_AA + C_RA; %Total
Res.

R_T = 0.5 * C_T * rho_h2o * S * v^2;

Pe = (R_T* v)/0.51; %0.51 efficiency from mech
to electrical
end

```

C. POWERSCRIPT FUNCTION

```

% %%% MODEL 4_based on current for Battery and
SuperCap
% % Regulation with sinusoidal exosystem.
% % x=[Q_tilde, Igen, Ibatt, SOCbatt-SOCrated,
Isc,SOC_SC]'
% % u=[DeltaPgen, DeltaIbatt, DeltaIsc]'

% %%% STATE SPACE MODEL

function
[e,x,u,w]=Powerscript(I_wave,w1,w2,theta0,FS,Ig
en,t,Voc,Q_batt,Vmax,SC_Cap,T_wave);

Ts = 1/FS

gamma = -(T_wave/(3600*200)) % Large gamma =
battery size smaller %200
beta = -(T_wave / (Vmax*45*7)) % , S C =
0.00001 , 5 parallel branches

F = [0.8, 1, 1,0,1,0 ;
0, 1, 0,0, 0, 0 ;
0, 0, 1, 0, 0, 0 ;
0, 0, gamma, 1,0,0;
0, 0, 0, 0, 1, 0

```

```

0, 0, 0, 0,beta,1];

G = [ 0,0,0;
1,0,0;
0,1,0;
0,0,0;
0,0,1;
0,0,0];

B = [-1, 0;
0, 0;
0, 0;
0, 0;
0, 0;
0, 0];

H = [0, 1, 1,0,1,0];
J = [ 0,0,0];
D = [-1,0];

% EXOSYSTEM
A=[cos(theta0), -sin(theta0); sin(theta0),
cos(theta0)];

%%%%%%%%%%%%%%%%%%%%%%%%%%%%%%%%%%%%%%%%%%%%%%%%%%%%%%%%%%%%%%%%%%%%%%%%

% dimensions
Nx=size(F,1); % state size
Nu=size(G,2); % input size
Ny=size(H,1); % output size
Nw=size(A,1); % exosystem state size

%% Cost Parameters
%the higher the cost means, more peantly, less
use

```

```

rg=1; rbatt=1; rsc=1;% less weight on the rate
of change for the delta values as we want them
to go to steady state quicker

qxcv=1; % weight on the error (velocity) higher
= lower ripple in the error
qgen = 50; % weight on generator

qIbatt =50;% weight on battery %the battery has
give out more power as compared to geny %
inverse to qsoc
qSOC_batt=1; % weight on Battery SOC %

qISC = 1; %
qSOC_SC =1;

% Since  $|e|^2 = z'C'Cz + v'D'Dv + 2z'C'Dv$  then
diag_q = [qxcv qgen qIbatt qSOC_batt qISC
qSOC_SC];
%  $Q = qe * H' * H$ ;
Q=diag(diag_q)+(H'*H);
R=diag([rg,rbatt,rsc])+qxcv*J'*J;
E=qxcv*H'*J;

% Riccati Equation
[K,P,CLP]=dlqr(F,G,Q,R,E);

%x(t)
Igen_max = inf%100 %100;% bounds on Igen no
bounds on the generators , so to get a quicker
system reponses as well as to see the effect on
the rae of change of the gen
Igen_min = inf%100; %bounds on Igen

%Battery constraints

% assuming the Battery starts at 50%, 50% = 0

```

```

%rate of change for SOC for the batteries..
time to reach steady state ,
DSOC_batt_max= 0.8 ;%max 90%
DSOC_batt_min= 0;%-0.2;% min 20%

Ibatt_max = 800 %400 % mac discharge is 400A
Ibatt_min = 800

%Super_cap Constraints

ISC_max = 240*4;
ISC_min = 240*4;

% assuming the Supercapacitor starts at 50%,
50% = 0
SC_SOC_max = 0.9; %
SC_SOC_min = -0.1;%

% constraints on output XV

Xv_min = 20; % constraints on the error in
Q_tilde, speed vary
XV_max = 20;

Ax=[0,0,1,0,0,0; % IBattery
    0,0,-1,0,0,0; % IBattery
    0,1,0,0,0,0; % Gen
    0,-1,0,0,0,0; % Gen
    0,0,0,1,0,0; % Battery SOC
    0,0,0,-1,0,0; % Battery SOC
    0,0,0,0,1,0; % ISuperCap
    0,0,0,0,-1,0; % ISuperCap
    0,0,0,0,0,1; % SuperCap_SOC
    0,0,0,0,0,-1; % SuperCap_SOC
    1,0,0,0,0,0; % XV
    -1,0,0,0,0,0]; % XV

```

```

bx=[Ibatt_max;Ibatt_min;Igen_max;Igen_min;DSOC_
batt_max;DSOC_batt_min;ISC_max;ISC_min;SC_SOC_m
ax;SC_SOC_min;XV_max;Xv_min]; %

% Constraints on Variables
% u(t)
DPgen_max=50 ; % max on |DeltaPgen| % should be
the rate of change for delta Pgen .. Smaller
Dpgen Max, slower rate of change for the
generator
% the lower the value for DPgen, the slower it
will reach a steady state value

DPbatt= 500;
DPSC = 5000;

Au=[1,0,0; % Constraint on the Generator rate
on change of
-1,0,0;
0,1,0;
0,-1,0;
0,0,1;
0,0,-1]; % Constraint on the Generator rate on
change of
bu=[DPgen_max;DPgen_max;DPbatt;DPbatt;DPSC;DPSC
];

N=20; % length of Prediction Horizon, 2 sample
wave, based on the sampling Frequency

[Linv,Fmpc,Gu,Hu,hu, options,
iA0]=mpcsetup(N,F,G,Q,R,E,P,Ax,bx,Au,bu);

% Solve Francis Equation
% T is Nx by Nw, L is Nu by Nw
[T,L]=Francis(F,G,H,J,A,B,D,Nx,Nu,Ny,Nw);

```

```

% Check Francis Equation: these terms should be
zero
F*T+G*L+B-T*A;
H*T+J*L+D;

% Constraints on  $v=u-Lw$  are of the form
 $Gu*V < Hu*z(t)+hu+Hw*w(t)$ 
% Just follow the notes:
Hw=[];
for k=1:N
    Hw=[Hw;-Ax*T*A^k];
end
for k=1:N
    Hw=[Hw;-Au*L*A^k];
end

%%%%%%%%%%%%%%%%%%%%%%%%%%%%%%%%%%%%%%%%%%%%%%%%%%%%%%%%%%%%%%%%%%%%%%%%
%%% MPC Control Simulation

Nsim=length(t)+1; % length of simulation
n=1:Nsim;

% Initial State
x(:,1)=[0;w1(1);0;0;0;0]; % Q tilde, Pgen,
IBatt, SOC_B, ISC,SOC_SC
w(:,1)=[w1(1);w2(1)];
z(:,1)=x(:,1)-T*w(:,1);

for t=1:Nsim-1;

    [V, status, iA, lambda] = mpcqpsolver(Linv,
Fmpc'*z(:,t), -Gu, -Hu*z(:,t)-hu-Hw*w(:,t),
double.empty(0,1), double.empty(0,1),
iA0,options);
    v(:,t)=V(1:Nu); % MPC
    e(t)=H*z(:,t)+J*v(:,t);
    z(:,t+1)=F*z(:,t)+G*v(:,t);

```

```

w(:,t+1)=A*w(:,t);
% back to original x and u
x(:,t)=z(:,t)+T*w(:,t);
u(:,t)=v(:,t)+L*w(:,t);
end

end % End of Function

```

D. MPCSETUP FUNCTION

```

function [Linv,F,Gu,Hu,hu, options,
iA0]=mpcsetup(N,A,B,Q,R,E,P, Ax,bx,Au,bu)
% [Linv,F,Gu,Hu,hu, options,
iA0]=mpcsetup(N,A,B,Q,R,E,Ax,bx,Au,bu)
% by R. Cristi, 8/1/2019
% INPUTS:
% N=length of time horizon
% A,B = state equations
% Q,R,E= quadratic penalties for state,input
and crossterm (2x'Eu)
% P = last state penalty from ARE
% A_x, b_x, A_u, b_u constraints on x and u
% OUTPUTS:
% Optimization of U'HU+2x(t)'FU, w.r.t. U
% Linv=a Choleski representation of H
% Constraints of the form
% Gu*U<Hu*x(t)+hu
% options and iA0 parameters for the algorithm,
given as default.
% At each iteration "t" call the algorithm
% [U, status, iA, lambda] = mpcqpsolver(Linv,
F'*x(:,t), -Gu, -Hu*x(:,t)-hu,
double.empty(0,1), double.empty(0,1),
iA0,options);
% u(:,t)=U(1:Nu); % Nu=size(B,2), number of
inputs
%%%%%%%%%%%%%%%%%%%%%%%%%%%%%%%%%%%%%%%%%%%%%%%%%%%%%%%%%%%%%%%%%%%%%%%%

```

```

%%%%%%%%%%
Nx=size(A,1); % dimension of the state
Nu=size(B,2); % number of inputs

%%%% Matrix Sx

Sx=eye(Nx);
for k=1:N
    Sx=[Sx; A^k];
end

%%%%%%%% Matrix Su
Suk=zeros(Nx, Nu*N); % first block
Su=Suk;
for k=1:N
    Suk=[(A^(k-1))*B, Suk(:,1:(end-Nu))];
    Su=[Su;Suk];
end

% Matrices Qbar, Rbar, Ebar
% Note: use "kronecker" product to form block
diagonal matrices:
Qbar=kron(diag([ones(1,N),0]),
Q)+kron(diag([zeros(1,N), 1]), P);
Rbar=kron(eye(N), R);
Ebar=kron(eye(N), E);
% Sxbar, Subar in the notes:
SufirstN=Su(1:N*Nx, :); SxfirstN=Sx(1:N*Nx,:);
% first N locks
% Sx, Su underlined in the notes:
SulastN=Su(Nx+1:end, :);
SxlastN=Sx(Nx+1:end,:); % last N blocks

% Matrices H,F,Y

```

```

H=Su'*Qbar*Su+Rbar+SufirstN'*Ebar+Ebar'*Sufirst
N;
F=Sx'*Qbar*Su+SxfirstN'*Ebar;
Y=Sx'*Qbar*Sx;

% Setup Constraints of the form
%  $Gx \leq Hx + hx$ 
%  $Gu \leq Hu + hu$ 
% SxlastN, SulastN are Sx and Su without the
first block (ie the first Nx rown)

Axbar=kron(eye(N), Ax);
bxbar=kron(ones(N,1), bx);
Aubar=kron(eye(N), Au);
bubar=kron(ones(N,1), bu);

% constraints of input U from state x:
%  $Gx \leq Hx + hx$ 
Gx=Axbar*SulastN;
Hx=-Axbar*SxlastN;
hx=bxbar;

% total constraints on U:
% append constraints Aubar*U<bubar to
constraints from X:
%  $Gu \leq Hu + hu$ 
Gu=[Gx;Aubar];
Hu=[Hx; zeros(size(Aubar,1), Nx)];
hu=[hx;bubar];

%% Parameters for mpcQPsolver
Ng=size(Gu,1); % number of constraints

% Choleski decomposition for H
L = chol(H, 'lower');
Linv = L\eye(size(H,1));

```

```

% SET options for "mpqpccsolver" (in 2019b, just
copy from default in help file):
options.DataType='double';
options.MaxIter=200;
options.IntegrityChecks=true;
options.FeasibilityTol=1.0e-06;
options.Integrity.Checks=true;
iA0=false(Ng,1);
% END

```

E. FRANCIS FUNCTION

```

function
[T,L]=Francis(F,G,H,J,A,B,D,nx,nu,ny,nw)
% This function returns the solution of
% the discrete time Francis equations of
% linear regulation.
%  $F \cdot T + G \cdot L + B = T \cdot A$ 
%  $H \cdot T + J \cdot L + D = 0$ 
%
% The plant state is X which is NX dimensional.
% The plant control is U which is NU
dimensional.
% The plant output is Y which is NY
dimensional.
% The exosystem state is X_ which is NW
dimensional.
% The plant dynamics is
%  $x^+ = F \cdot x + G \cdot u + B \cdot w$ 
% The plant output is
%  $y = H \cdot x + J \cdot u + D \cdot w$ 
% The exosystem dynamics is
%  $w^+ = A \cdot w$ 
% If there is no unique solution to the Francis
equations
% then a least squares solution is found.
% The result will be unsatisfactory

```

```

% if NY>NU.
%

% We use the identity
%  $(A*Z*B)_{rs} = Z_{rs} * \text{kron}(A', B)$ 
% where A, Z, B are matrices of dimensions
% compatible for multiplication
% and rs means row stacked.

temp1=kron([F,G;H,J].',eye(nw));
temp2=temp1-
kron([eye(nx),zeros(nx,nu);zeros(ny,nx+nu)].',A
);
temp=-reshape([B;D].',1,(nx+ny)*nw);
temp=temp*pinv(temp2);
T=reshape(temp(1,1:nx*nw),nw,nx).';
L=reshape(temp(1,nx*nw+1:(nx+nu)*nw),nw,nu).';

% Copyright A. J. Krener 2019, Second Reader

```

THIS PAGE INTENTIONALLY LEFT BLANK

LIST OF REFERENCES

- [1] United Nations Conference on Trade and Development, “Review of maritime transport 2015,” UNCTD, Geneva, Switzerland, Rep. UNCTAD/RMT/2015, 2015. [Online]. Available: <https://unctad.org/en/pages/PublicationWebflyer.aspx?publicationid=1374>
- [2] World Trade Organization, “WTO Statistics: Trade and tariff data.” Accessed: Jan. 25, 2020. [Online]. Available: https://www.wto.org/english/res_e/statis_e/statis_e.htm
- [3] A. Boveri, F. Silvestro, M. Molinas, and E. Skjong, “Optimal sizing of energy storage systems for shipboard applications,” *IEEE Trans. Energy Convers.*, vol. 34, no. 2, pp. 801–811, Jun. 2019. [Online]. doi: 10.1109/TEC.2018.2882147
- [4] International Maritime Organization, “Energy efficiency and the reduction of GHG emissions from ships.” Accessed Jan. 25, 2020. [Online]. Available: <http://www.imo.org/en/MediaCentre/HotTopics/GHG/Pages/default.aspx>
- [5] M. Mara et al., *Regulating air emissions from ships the state of the art on methodologies, technologies and policy options*. Luxembourg, Belgium: Publications Office, 2011.
- [6] P. Tran, “France orders hybrid ships for its Navy,” *Defense News*, Mar. 14, 2018. [Online]. Available: <https://www.defensenews.com/industry/techwatch/2018/03/14/france-orders-hybrid-ships-for-its-navy/>
- [7] The Government of the United Kingdom, “UK & USA test naval power systems,” Gov.uk, May 1, 2019. [Online]. Available: <https://www.gov.uk/government/news/uk-usa-test-naval-power-systems>
- [8] U.S. Navy, “The U.S. Navy.” Accessed Jan. 25, 2020. [Online]. Available: https://www.navy.mil/navydata/nav_legacy.asp?id=145
- [9] M. U. Mutarraf, Y. Terriche, K. A. K. Niazi, J. C. Vasquez, and J. M. Guerrero, “Energy storage systems for shipboard microgrids—A review,” *Energies*, vol. 11, no. 12, p. 3492, Dec. 2018. [Online]. doi: 10.3390/en11123492
- [10] R. D. Geertsma, R. R. Negenborn, K. Visser, and J. J. Hopman, “Design and control of hybrid power and propulsion systems for smart ships: A review of developments,” *Appl. Energy*, vol. 194, pp. 30–54, May 2017. [Online]. doi: 10.1016/j.apenergy.2017.02.060

- [11] K. Ralson, “Behavior/application of supercapacitors integrated with a ship’s power management system during varying load conditions,” M.S. thesis, Dept. of ECE, NPS, Monterey, CA, USA, 2019.
- [12] C. Kim, E. NamGoong, S. Lee, T. Kim, and H. Kim, “Fuel economy optimization for parallel hybrid vehicles with CVT,” *SAE Trans.*, vol. 108, pp. 2161–2167, 1999. [Online]. Available: <https://www.jstor.org/stable/44733866?seq=1>
- [13] G. Paganelli, G. Ercole, A. Brahma, Y. Guezennec, and G. Rizzoni, “General supervisory control policy for the energy optimization of charge-sustaining hybrid electric vehicles,” *JSAE Rev.*, vol. 22, no. 4, pp. 511–518, Oct. 2001. [Online]. doi: 10.1016/S0389-4304(01)00138-2
- [14] U. Zoelch and D. Schroeder, “Dynamic optimization method for design and rating of the components of a hybrid vehicle,” *Int. J. Veh. Des.*, vol. 19, no. 1, pp. 1–13, Jan. 1998. [Online]. doi: 10.1504/IJVD.1998.062090
- [15] C.-C. Lin, H. Peng, J. W. Grizzle, and J.-M. Kang, “Power management strategy for a parallel hybrid electric truck,” *IEEE Trans. Control Syst. Technol.*, vol. 11, no. 6, pp. 839–849, Nov. 2003. [Online]. doi: 10.1109/TCST.2003.815606
- [16] M. Koot, J. T. B. A. Kessels, B. deJager, W. P. M. H. Heemels, P. P. J. vandenBosch, and M. Steinbuch, “Energy management strategies for vehicular electric power systems,” *IEEE Trans. Veh. Technol.*, vol. 54, no. 3, pp. 771–782, May 2005. [Online]. doi: 10.1109/TVT.2005.847211
- [17] P. Poramapojana, “Predictive control of hybrid vehicle powertrain for intelligent energy management,” M.S. thesis, Dept. of Mech. Eng.-Eng. Mechanics, Michigan Tech, USA, 2012. [Online]. Available <https://digitalcommons.mtu.edu/etd-restricted/61/>
- [18] S. Di Cairano and I. V. Kolmanovsky, “Automotive applications of model predictive control,” in *Handbook of Model Predictive Control*, S. V. Raković and W. S. Levine, Eds. Cham, Switzerland: Springer International Publishing, 2019, pp. 493–527.
- [19] P. Ortner and L. del Re, “Predictive control of a diesel engine air path,” *IEEE Trans. Control Syst. Technol.*, vol. 15, no. 3, pp. 449–456, May 2007. [Online]. doi: 10.1109/TCST.2007.894638
- [20] M. Iwadare, M. Ueno, and S. Adachi, “Multi-variable air-path management for a clean diesel engine using model predictive control,” ResearchGate. [Online]. Accessed Jan. 13, 2020. Available: https://www.researchgate.net/publication/277671100_Multi-Variable_Air-Path_Management_for_a_Clean_Diesel_Engine_Using_Model_Predictive_Control

- [21] G. Ripaccioli, A. Bemporad, F. Assadian, C. Dextreit, S. Di Cairano, and I. V. Kolmanovsky, “Hybrid modeling, identification, and predictive control: An application to hybrid electric vehicle energy management,” in *Hybrid Systems: Computation and Control*, Berlin, Heidelberg: Springer, 2009, pp. 321–335. [Online]. doi: 10.1007/978-3-642-00602-9_23
- [22] H. Alafnan *et al.*, “Stability improvement of DC power systems in an all-electric ship using hybrid SMES/battery,” *IEEE Trans. Appl. Supercond.*, vol. 28, no. 3, pp. 1–6, Apr. 2018. [Online]. doi: 10.1109/TASC.2018.2794472
- [23] A. Subic, F. Schiavone, M. Leary, and J. Manning, “Comparative life cycle assessment (LCA) of passenger seats and their impact on different vehicle models,” *Int. J. Veh. Des.*, vol. 53, May 2010. [Online]. doi: 10.1504/IJVD.2010.032985.
- [24] Vesseltracker, “Oppedal - Passenger ship, IMO 9419216, MMSI 258221500, Callsign LAOA, Flag Norway,” vesseltracker.com. [Online]. Accessed Jan. 8, 2020. Available: <https://www.vesseltracker.com/en/Ships/Oppedal-9419216.html>.
- [25] M. U. Mutarraf, Y. Terriche, K. A. K. Niazi, J. C. Vasquez, and J. M. Guerrero, “Energy storage systems for shipboard microgrids—A review,” *Energies*, vol. 11, no. 12, p. 3492, Dec. 2018. [Online]. doi: 10.3390/en11123492
- [26] A. Kwasinski, W. Weaver, and R. S. Balog, *Microgrids and Other Local Area Power and Energy Systems*. Cambridge, UK: Cambridge University Press, 2016.
- [27] Capacitor Guide, “Types.” Accessed Feb. 19, 2020. [Online]. Available: <http://www.capacitorguide.com/tag/types/>
- [28] A. Khaligh and Z. Li, “Battery, ultracapacitor, fuel cell, and hybrid energy storage systems for electric, hybrid electric, fuel cell, and plug-in hybrid electric vehicles: State of the art,” *IEEE Trans. Veh. Technol.*, vol. 59, no. 6, pp. 2806–2814, Jul. 2010. [Online]. doi: 10.1109/TVT.2010.2047877
- [29] J. Cao and A. Emadi, “A new battery/ultracapacitor hybrid energy storage system for electric, hybrid, and plug-in hybrid electric vehicles,” *IEEE Trans. Power Electron.*, vol. 27, no. 1, pp. 122–132, Jan. 2012. [Online]. doi: 10.1109/TPEL.2011.2151206
- [30] L. Kouchachvili, W. Yaïci, and E. Entchev, “Hybrid battery/supercapacitor energy storage system for the electric vehicles,” *J. Power Sources*, vol. 374, pp. 237–248, Jan. 2018. [Online]. doi: 10.1016/j.jpowsour.2017.11.040
- [31] T. I. Bø and T. A. Johansen, “Battery power smoothing control in a marine electric power plant using nonlinear model predictive control,” *IEEE Trans. Control Syst. Technol.*, vol. 25, no. 4, pp. 1449–1456, Jul. 2017. [Online]. doi: 10.1109/TCST.2016.2601301

- [32] W. Jing, C. Hung Lai, S. H. W. Wong, and M. L. D. Wong, "Battery-supercapacitor hybrid energy storage system in standalone DC microgrids: A review," *IET Renew. Power Gener.*, vol. 11, no. 4, pp. 461–469, Mar. 2017. [Online]. doi: 10.1049/iet-rpg.2016.0500
- [33] J. Li, B. Cornelusse, P. Vanderbemden, and D. Ernst, "A SC/battery hybrid energy storage system in the Microgrid," *Energy Procedia*, vol. 142, pp. 3697–3702, Dec. 2017. [Online]. doi: 10.1016/j.egypro.2017.12.264
- [34] Z. Jingnan and Z. Ying, "Control strategy of hybrid energy storage system in ship electric propulsion," in *2018 IEEE Int. Conf. Mechatronics & Autom. (ICMA)*, Changchun, PRC, 2018, pp. 1026–1030. [Online]. doi: 10.1109/ICMA.2018.8484339
- [35] The Project Definition, "Load Levelling," theprojectdefinition.com, Dec. 5, 2015. [Online]. Available: <https://www.theprojectdefinition.com/load-levelling/>
- [36] N. Sonoda, H. Matsunaga, T. Gengo, M. Minami, M. Oishi, and T. Hashimoto, "Development of containerized energy storage system with lithium-ion batteries," *Add name of journal*, vol. 50, no. 3, p. 6, 2013.
- [37] O. Simona, S. Lorenzo, and G. Rizzoni, *Hybrid Electric Vehicles - Energy Management Strategies*, 1st ed., New York, NY, USA: Springer, 2016.
- [38] A. Ali and D. Söffker, "Towards optimal power management of hybrid electric vehicles in real-time: A review on methods, challenges, and state-of-the-art solutions," *Energies*, vol. 11, no. 3, p. 476, Feb. 2018. [Online]. doi: 10.3390/en11030476
- [39] T. Hofman, M. M. Steinbuch, R. M. V. Druten, and A. Serrarens, "Rule-based energy management strategies for hybrid vehicles," 2007. [Online]. doi: 10.1504/IJEHV.2007.014448
- [40] P. Zhang, F. Yan, and C. Du, "A comprehensive analysis of energy management strategies for hybrid electric vehicles based on bibliometrics," *Renew. Sustain. Energy Rev.*, vol. 48, pp. 88–104, Aug. 2015. [Online]. doi: 10.1016/j.rser.2015.03.093
- [41] P. E. Orukpe, "Model predictive control fundamentals," *Niger. J. Technol.*, vol. 31, no. 2, p. 10. 2012. [Online]. Available: <https://www.semanticscholar.org/paper/Model-Predictive-Control-Fundamentals-Orukpe/583a37f7bb074286f6ec92e20eac259f20cae938>
- [42] J. Rodriguez and P. Cortes, *Predictive Control of Power Converters and Electrical Drives*. Chichester, UK: John Wiley & Sons, Ltd, 2012.

- [43] F. Borrelli, A. Bemporad, and M. Morari, *Predictive Control for Linear and Hybrid Systems*, 1st ed. Cambridge; New York, NY, USA: Cambridge University Press, 2017.
- [44] L. Wang, *Model Predictive Control System Design and Implementation Using MATLAB*. London, UK: Springer, 2009.
- [45] “MF Oppedal,” *Wikipedia*. Accessed Jan. 20, 2020. [Online]. Available: https://no.wikipedia.org/wiki/MF_%C2%ABOppedal%C2%BB
- [46] Fjord Ferries, “Fjord ferries in Norway.” Accessed Jan. 8, 2020. [Online]. Available: http://www.fjordfaehren.de/no_f2/nybygg2_norferjer_2008.htm
- [47] H. E. Guldhammer and S. A. Harvald, *Ship Resistance: Effect of Form and Principal Dimensions*. Copenhagen, Denmark: Akademisk Forlag, 1970.
- [48] MAN Energy Solutions, “Basic principles of propulsion.” Accessed Feb. 26, 2020. [Online]. Available: <https://marine.man-es.com/propeller-aft-ship/basic-principles-of-propulsion>
- [49] International Towing Tank Conference, “1978 ITTC performance prediction method.” [Online]. Available: <https://itc.info/media/1593/75-02-03-014.pdf>.
- [50] The Engineering Toolbox, “Froude Number.” Accessed Jan. 8, 2020. [Online]. Available: https://www.engineeringtoolbox.com/froude-number-d_578.html
- [51] M. Lützen and H. O. H. Kristensen, “A model for prediction of propulsion power and emissions – Tankers and bulk carriers,” World Maritime Technology Conference, Saint-Petersburg, Russia p. 13, May 2012.
- [52] U.S. Naval Academy, “Chapter 7 Resistance and Powering of Ships,” class notes for EN 400: Principles of Ship Performance, U.S. Naval Academy, Annapolis, MD, USA, p. 46. [Online]. Available: https://www.usna.edu/NAOE/_files/documents/Courses/EN400/02.07%20Chapter%207.pdf
- [53] Y. Kim, J. Koh, Q. Xie, Y. Wang, N. Chang, and M. Pedram, “A scalable and flexible hybrid energy storage system design and implementation,” *J. Power Sources*, vol. 255, pp. 410–422, Jun. 2014. [Online]. doi: 10.1016/j.jpowsour.2013.12.102
- [54] L. Gao, R. A. Dougal, and S. Liu, “Power enhancement of an actively controlled battery/ultracapacitor hybrid,” *IEEE Trans. Power Electron.*, vol. 20, no. 1, pp. 236–243, Jan. 2005. [Online]. doi: 10.1109/TPEL.2004.839784

- [55] N. R. Tummuru, M. K. Mishra, and S. Srinivas, “Dynamic energy management of renewable grid integrated hybrid energy storage system,” *IEEE Trans. Ind. Electron.*, vol. 62, no. 12, pp. 7728–7737, Dec. 2015, doi: 10.1109/TIE.2015.2455063
- [56] H. Yin, C. Zhao, M. Li, and C. Ma, “Utility function-based real-time control of a battery ultracapacitor hybrid energy system,” *IEEE Trans. Ind. Inform.*, vol. 11, no. 1, pp. 220–231, Feb. 2015, doi: 10.1109/TII.2014.2378596.
- [57] Y. Tang and A. Khaligh, “On the feasibility of hybrid battery/ultracapacitor energy storage systems for next generation shipboard power systems,” in *2010 IEEE Vehicle Power and Propulsion Conference*, 2010, pp. 1–6. [Online]. doi: 10.1109/VPPC.2010.5729211
- [59] Corvus Energy, “Corvus Moray Power.” Accessed Jan. 24, 2020. [Online]. Available: <https://corvusenergy.com/products/corvus-moray-power/>
- [60] Maxwell Technologies, “Maxwell Technologies 125 volt transportation modules ultracapacitors application specific modules.” Accessed Jan. 18, 2020. [Online]. Available: <https://www.maxwell.com/products/ultracapacitors/125v-tran-modules>
- [61] Tecate Group, “Ultracapacitor frequently asked questions.” Accessed Jan./ 29, 2020. [Online]. Available: <https://www.tecategroup.com/products/ultracapacitors/ultracapacitor-FAQ.php>
- [62] MATLAB, “Solve a quadratic programming problem using the KWIK algorithm - MATLAB mpcqpsolver.” Accessed Feb. 2, 2020. [Online]. Available: <https://www.mathworks.com/help/mpc/ref/mpcqpsolver.html#d117e14529>
- [63] C. O. Aguilar and A. J. Krener, “Model predictive regulation,” October 26, 2013. [Online]. *ArXiv13107135 Math*

INITIAL DISTRIBUTION LIST

1. Defense Technical Information Center
Ft. Belvoir, Virginia
2. Dudley Knox Library
Naval Postgraduate School
Monterey, California